Geothermics 96 (2021) 102146

Contents lists available at ScienceDirect

Geothermics

journal homepage: www.elsevier.com/locate/geothermics

Soft stimulation treatment of geothermal well RV-43 to meet the growing heat demand of Reykjavik

Hannes Hofmann [a,*], Günter Zimmermann [a], Ernst Huenges [a], Simona Regenspurg [a], Santiago Aldaz [a], Claus Milkereit [a], Sebastian Heimann [a], Torsten Dahm [a,b], Arno Zang [a,b], Francesco Grigoli [c,d], Dimitrios Karvounis [c], Marco Broccardo [c,e], Stefan Wiemer [c], Vala Hjörleifsdóttir [f], Bjarni Reyr Kristjánsson [f], Gylfi Páll Hersir [g], Ragnheiður St. Ásgeirsdóttir [g], Rögnvaldur Magnússon [g], Sigurveig Árnadóttir [g]

[a] Helmholtz Centre Potsdam GFZ German Research Centre for Geosciences, Telegrafenberg, 14473 Potsdam, Germany
[b] University of Potsdam, Am Neuen Palais 10, 14469 Potsdam, Germany
[c] Swiss Seismological Service, ETH Zurich, Sonneggstrasse 5, 8092 Zurich, Switzerland
[d] University of Pisa, Via Santa Maria 53, 56126 Pisa, Italy
[e] University of Trento, Via Mesiano 77, 38123 Trento, Italy
[f] Reykjavik Energy, Bæjarháls 1, 110 Reykjavík, Iceland
[g] Iceland Geosurvey (ÍSOR), Grensásvegi 9, 108 Reykjavík, Iceland

ARTICLE INFO

Keywords:
Cyclic soft stimulation
Multi-stage hydraulic stimulation
Zonal isolation
Realtime seismic monitoring
Fluid injection induced seismicity
Adaptive traffic light system
enhanced geothermal systems (EGS)

ABSTRACT

Reykjavik is almost entirely heated by geothermal energy. Yet, recent growth of the city significantly increased the heat demand. Past experiences in Iceland's capital region showed that hydraulic stimulation of existing geothermal wells is suited to improve hydraulic performance and energy supply. However, fluid injection may also trigger felt or even damaging earthquakes, which are of concern in populated areas and pose a significant risk to stimulation operations. Consequently, soft stimulation concepts have been developed to increase geothermal well performance while minimizing environmental effects such as induced seismicity. In a demonstration project of hydraulic soft stimulation in October 2019, more than 20.000 m^3 of water were injected into well RV-43 in Reykjavik in multiple stages and with different injection schemes. The hydraulic performance of the well was improved without inducing felt seismicity. An a priori seismic risk assessment was conducted and for the first time the risk was continuously updated by an adaptive traffic light system supported by a sophisticated realtime microseismic monitoring. Our results confirm that it is possible to improve the performance of geothermal wells in Reykjavik and worldwide with acceptable technical, economic, and environmental risks. Here we provide an overview of the entire stimulation project including site description, stimulation design, zonal isolation, logging, seismic risk assessment and mitigation measures, realtime seismic, hydraulic and chemical monitoring, and stimulation results and challenges.

1. Introduction

Geothermal energy provides 99.9% of the district heating load of Reykjavik, the capital city of Iceland (Gunnlaugsson et al., 2000). This energy is distributed through two separate networks. One network is fed by the two high temperature power plants Nesjavellir and Hellisheiði located ~20–30 km east of Reykjavik. The second network is fed by the three low temperature fields Laugarnes, Ellidaar, and Mosfellsbær located within or near the city limits. The growing population and tourist sector push the current network at its limit. In particular, additional low temperature heat sources need to be accessed to ensure a reliable heat provision for the city center that is supplied by the low temperature network. To achieve this, new low temperature wells can be drilled, or the productivity of existing wells can be improved, for example by hydraulic stimulation treatments, where water is injected into the low permeability rock mass to improve existing flow paths and develop new ones. While the operator Reykjavik Energy considers both, drilling and stimulation, the demonstration of a safe and reliable method

* Corresponding author.
E-mail address: hannes.hofmann@gfz-potsdam.de (H. Hofmann).

https://doi.org/10.1016/j.geothermics.2021.102146
Received 3 February 2021; Received in revised form 19 April 2021; Accepted 17 May 2021
Available online 9 June 2021

for hydraulic stimulation as productivity enhancement technique for Reykjavik is subject of this study. The ~1.55 km deep and 1.82 km long well RV-43 on the peninsula Geldinganes was chosen as representative demonstration site.

Hydraulic stimulation has been a routine procedure to improve the productivity of low temperature geothermal wells in Reykjavik since the 1970s with at least 38 stimulated wells only in Mosfellsbær (Tomasson and Thorsteinsson, 1978). Additional hydraulic stimulations in Reykjavik are reported for the Seltjarnes area (Tulinius et al., 1996) and Haimson and Voight (1977) performed two scientific hydraulic fracturing treatments in Reykjavik at shallow depths for stress determination. According to Tomasson and Thorsteinsson (1978), hydraulic stimulations were typically performed with single packers, injection rates of 15 to 100 l/s and wellhead pressures (WHP) up to 15 MPa. Compared to the estimates obtained after drilling, but before stimulation, this resulted in a thirty to forty-fold productivity improvement. Compared to productivity estimates from the total loss of circulation during drilling the improvement was up to three-fold. This productivity increase was attributed to re-opening of production zones that were plugged during drilling, removal of zeolite and calcite vein deposits and permeability increase of hyaloclastites intersecting the wells.

Even though no seismic activity was reported in relation to any of these fluid injection activities, there was also very limited seismic monitoring in place and prominent cases of induced seismicity from around the world (e.g., Giardini, 2009; Grigoli et al., 2018a; Lee et al., 2019) have highlighted that emphasis must be given to seismic risk assessment and mitigation in geothermal projects in general. The potential seismic risk of the stimulation of RV-43 was considered also by the operator, because Reykjavik is the most populated area of Iceland.

Although the population in Iceland is familiar with earthquakes due to their location at a plate boundary, recent induced earthquakes in a geothermal field near Hellisheiði had caused concern (Bessason et al., 2012; Flóvenz et al., 2015). An overview of induced seismicity in geothermal reservoirs is given for example by Zang et al. (2014) and Buijze et al., 2019. The maximum allowable seismic magnitude must be determined for each site individually through a detailed process of risk assessment (Majer et al., 2012). It depends on the peak ground velocity at the surface, the local geology, and surface structures. One option is to keep seismicity so low that it is not perceptible by humans on the surface. For this, Westaway and Younger (2014) suggest for the UK that the existing regulatory limits applicable to quarry blasting (i.e. peak ground velocities in the seismic wave field incident on any residential property of 10 mm/s during the working day, 2 mm/s at night, and 4.5 mm/s at other times) could be readily applied to cover such induced seismicity. Another option is to use seismic traffic light systems, which are widely accepted as risk mitigation procedures for hydraulic treatments (Bommer et al., 2015; Maxwell et al., 2015). Such concepts have been applied in the field of EGS; early examples are the case of the Berlin geothermal field in El Salvador (Bommer et al., 2006) and the Basel EGS stimulation in Switzerland (Häring et al., 2008). Magnitude thresholds are also used in next-generation advanced or adaptive traffic-light systems (Wiemer et al., 2017). In traffic-light systems, either fluid injection is stopped, the treatment pressure is reduced, or the well is shut in or flowed back if certain thresholds of seismic magnitudes are exceeded during injection (Baisch et al., 2019).

To demonstrate safe and economically viable strategies for reservoir stimulation near urban areas, we deployed so-called “hydraulic soft stimulation treatments” of the Geldinganes geothermal reservoir. Soft stimulation treatments (Huenges et al., 2018) aim to achieve enhanced reservoir performance while minimizing environmental impacts such as induced seismicity. They have been tested in selected underground lab studies (Zang et al., 2017) as well as in demonstration projects (Hofmann et al., 2018a; 2019). Soft stimulation measures in general may include different hydraulic, thermal and chemical treatments. For the Geldinganes project hydraulic soft stimulation treatments were performed and no thermal or chemical treatments were applied. The hydraulic soft stimulation treatments were embedded in a comprehensive strategy for risk assessment and risk mitigation, building on and partially extending the existing best practice in these domains. These measures included publicly accessible long-term local seismic monitoring before, during and after the treatment (http://veitur.isor.is/eqview/), real-time seismic monitoring with an extended temporal local seismic network (Fig. 1), chemical monitoring of flowback water, publication of a seismic risk assessment before the stimulation (Broccardo et al., 2020), operation of the first of its kind adaptive traffic light system, zonal isolation for a multi-stage stimulation and cyclic injection schemes (Hofmann et al., 2018a).

2. Site description

The demonstration site is the undeveloped low temperature geothermal field Geldinganes, a peninsula within the city limits of Reykjavik. The exceptional geothermal gradient of up to 450 °C/km on Geldinganes triggered the drilling of the 1550 m deep and 1832 m long well RV-43 in 2001 (Fig. 2). The well was drilled in a presumed fault above a magnetic anomaly interpreted as a deep gabbro body (Steingrímsson et al., 2001). While the required temperatures of >100 °C were found, flow rates were insufficient for economic fluid production. The initial production rate could be increased by an open hole stimulation treatment that was performed directly after drilling in 2001, but the well was still considered to be uneconomic. Currently, this field is re-assessed for development with new production wells. To additionally enhance the production, improve the local geological knowledge of the area, re-gain knowledge on hydraulic stimulation procedures in low temperature wells in Reykjavik, and demonstrate soft stimulation procedures, hydraulic stimulation tests were performed in well RV-43 in October 2019.

2.1. Regional structural geology

The rock below Geldinganes and its surroundings is highly fractured.

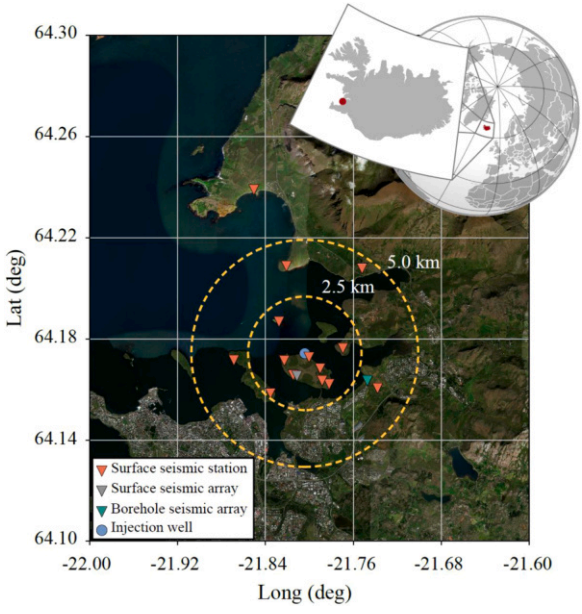

Fig. 1. Microseismic network of Geldinganes (Iceland). The network consists of 13 surface seismic three component (3C) stations, one surface array of 7 3C stations and one deep borehole geophone chain of 17 3C sensors. The Injection well is represented by the blue circle, while the two yellow circles with radii of 2.5 and 5.0 km, represent the internal and the external domain respectively. Note that during the stimulation periods the geophone chain was not in operation.

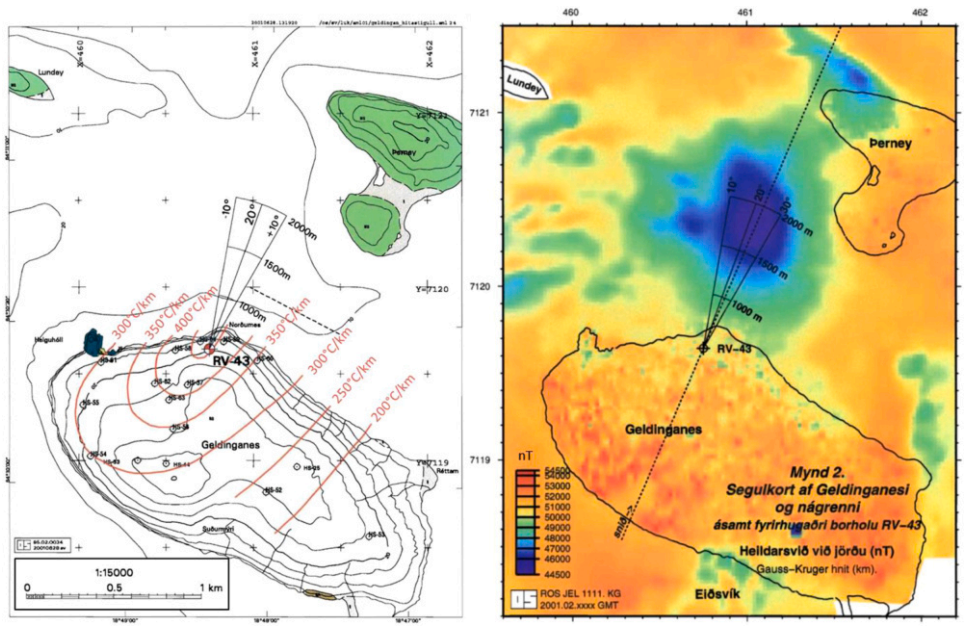

Fig. 2. Temperature contours based on 13 shallow boreholes (most of which are 100 – 120 m deep) show a NE-SW-trending (~N40°E) temperature anomaly that may indicate a fault zone (left, adapted from Steingrímsson et al., 2001) and magnetic map showing a low magnetization that is interpreted as a gabbro body (right, from Gunnarsson, 2001).

Surface lineaments near well RV-43 (Fig. 3) indicate the presence of two (sub)-vertical sets of normal faults dipping towards W to NW (Gudmundsson et al., 1992), a major NE-SW striking fault set (N42°E ± 8°) and a less prominent N-S striking fault set (N5°E ± 3°; data digitized from Sæmundsson et al., 2016). On the peninsula no faults were mapped, but shallow temperature measurements show an increased temperature gradient along a similar strike as fault set 1 (Figs. 2 and 3), which is also similar to the strike of regional faults (Sæmundsson et al., 2016).

The surface geological analysis by Jefferis and Voight (1981) revealed similar trends for two major fracture sets with the NE-SW set being the dominant one. This set is subparallel to dikes and normal faults and is described as the best developed and oldest of the fracture sets. The average fracture spacing in this set is 81 cm and the average mineralized gap is 2.9 mm. Its origin is associated to geothermal activity and the regional NW extension in the active zone. A second set typically strikes E-W with more variability as compared to the NE set. Its average fracture spacing is 116 cm and the average mineralized gap is 1.0 mm. This set is younger, and its origin is speculated to be due to cooling. Both fracture sets are typically subvertical with an average dip of 87°W (±8°), they typically cut dikes and intrusions and most of the mineralized fractures in the two major fracture sets had gaps and were anastomosing. Average fracture lengths traced from aerial photographs were 140 m and the orientations of the two most prominent sets are between N20°E – N50°E and between N70°E and N90°E. The authors suggest an extensional origin for both major fracture sets, although oblique extension cannot be ruled out.

In summary, the area is intersected by at least two (sub-) vertical sets

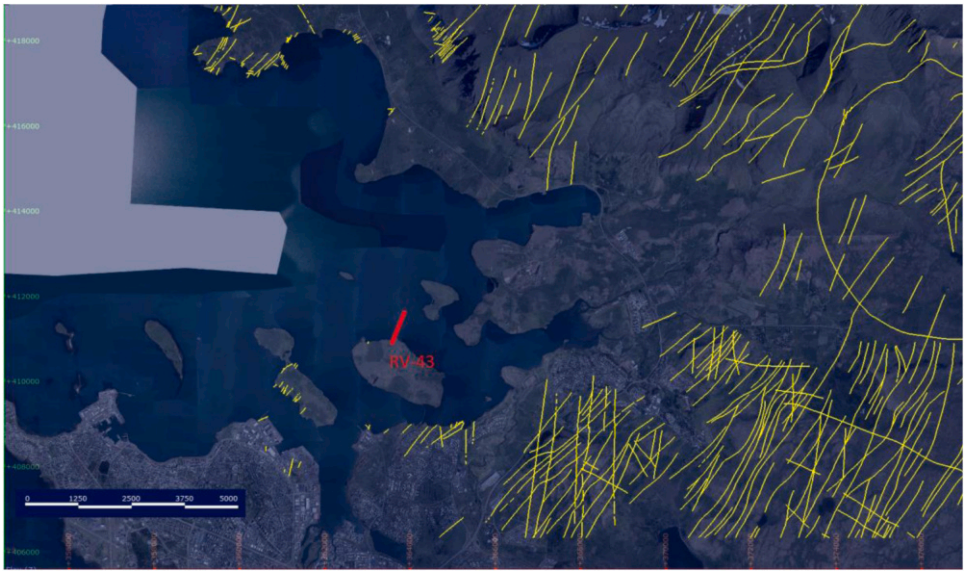

Fig. 3. Surface lineaments (yellow) from Sæmundsson et al. (2016) and path of well RV-43 (red) on Geldinganes. The (sub-)vertical normal faults may be divided into two sets striking ~N42°E and ~N5°E.

of normal faults and fractures striking ~N5°E and ~N40–50°E, respectively. The NW-SE striking set is the most prominent and has partially open fractures.

2.2. Stress field

Stress indicators for different depths from past analysis and new results presented in this manuscript are summarized in Fig. 4. They show that the stress regime is most likely strike-slip with potential local variations.

New pore pressure measurements on 25.10.2019 follow the same trend as earlier pressure measurements. The pore pressure gradient ΔPp is 9.66 MPa/km, represented by a fluid density of 985 kg/m^3 and a gravitational acceleration of 9.81 m/s^2. Haimson and Voight (1976) determined the stress gradients from four hydraulic fracturing tests in well H32 between 200 and 375 m TVD and from three hydraulic fracturing tests in well H18 between 180 and 324 m TVD. Both wells are located in Reykjavik. The vertical stress gradient for these wells was estimated to be 27 MPa/km. Due to the lack of density logs and petrophysical data from cores we assume the same vertical stress gradient for RV-43. The minimum horizontal stress gradient given by Haimson and Voight (1976) is 21 MPa/km. The maximum horizontal stress gradient given by Haimson and Voight (1976) is 3 MPa + 30 MPa/km. However, the scatter in the data is significant and extrapolation to depth difficult. A maximum principal stress of ~27 MPa was determined for the time when the NE trending fracture set was formed at ~1100 m depth (Jefferis and Voight 1981).

Intrusive Dolerites showed an increased SHmax magnitude as compared to hydraulic fracturing stress measurements in basalts in well H18 (Haimson and Voight, 1977). Haimson and Rummel (1982) found elevated stresses in thick lava flows by stress measurements in eastern Iceland. These zones may therefore serve as fracture height growth barriers and packer locations.

Based on stress inversions of focal mechanism solutions, geological indicators and one of the hydraulic fracturing stress measurements, the maximum horizontal stress direction in SW Iceland is primarily NE-SW (Gudmundsson et al., 1992; Heidbach et al., 2016; Ziegler et al., 2016). This is also supported by GPS measurements and resulting extensional and contractional horizontal strain rates (Keiding et al., 2009). Locally, this direction may vary between NW-SE and NE-SW as indicated by the hydraulic fracturing measurements in H18 and H32 in Reykjavik (Haimson and Voight, 1977). Based on the twelve stress indicators within a radius of ~10 km around the site with poor data quality (C-D), the maximum horizontal stress direction may range between N45°W and N37°E (Figure S1; Heidbach et al., 2016). The maximum horizontal stress direction in the paleostress field was determined to be between N20°E and N40°E based on fault slip data from SW Iceland (Gudmundsson et al., 1992).

2.3. Status of well RV-43

The deviated well RV-43 was drilled from 22 October 2001 until 24 November 2001 to a total measured depth (MD) of 1832 m and a true vertical depth (TVD) of ~1550 m. The average inclination and azimuth of the 1130 m long open hole section are ~38° and ~N20°E, respectively. The kick off point is at ~270 m and the horizontal distance between wellhead and bottom hole is ~810 m. Well completion, selected old and new well logs, interpreted geology, fracture zones and stimulation target intervals are summarized in Fig. 5. Three casings were installed: a 18 5/8″ surface casing from surface to 48 m MD, a 13 3/8″ anchor casing from surface to 252 m MD, and a 9 5/8“ production casing from 230 to 702 m MD, which is cemented from 702 to 400 m. The remainder of the well is open from 702 to 1832 m MD with a diameter of 8 ½”. In May 2019, the wellbore was not accessible by wireline logging tools below ~830 m MD, possibly due to a keyseat.

The largest part of well RV-43 intersects medium to coarse grained basalts (Fig. 5b). Above 200 m lavas and sediments are found along with some tuffs and breccias that erupted during glaciations. Below 200 m there are mostly doleritic intrusions, lavas and some layers of brecciated rocks. The intrusive rocks are usually less altered than their moderately to highly altered host rocks, which are lava piles. The intrusions however differ in alteration showing different relative ages of these rocks. The most abundant alteration minerals are pyrite, calcite and laumontite. The lithology changes in the bottom part of the well between ~1710–1810 m MD. The cuttings at this depth are comprised of anorthite, quartz and albite. This indicates that a gabbroic intrusion was intersected at this depth, probably the gabbro revealed NW of Geldinganes in the magnetic measurements (Fig. 2).

Almost no loss of circulation was observed during drilling. Some losses occurred below ~1700 m, but no large feed zones were identified. Minor feed zones were located at ~738 m, ~830 m, ~1030 m, ~ 1102 m, ~ 1135 m, ~1250 m, ~ 1330 m and ~1720 m MD based on

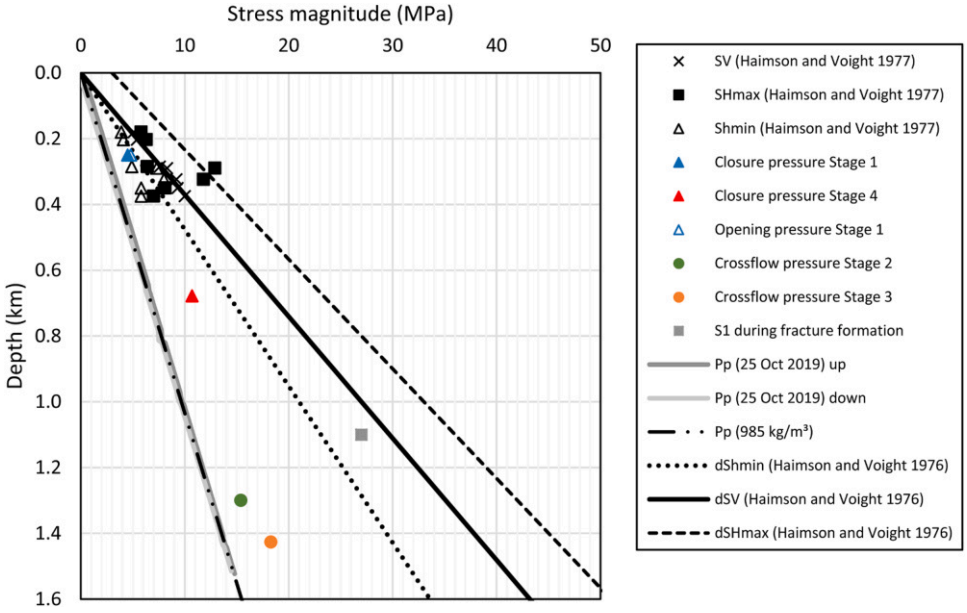

Fig. 4. Stress indicators derived from shallow borehole measurements from wells H18 and H32 (point data from Table 4 in Haimson and Voight (1977), stress gradients from Haimson and Voight (1976), maximum principal stress magnitude S1 during formation of natural fractures from Jefferis and Voight (1981)) and from the hydraulic stimulation of well RV-43 presented in this manuscript. Closure pressure is an approximation of the minimum principal stress and crossflow pressure is the pressure at which crossflow around the packer was observed.

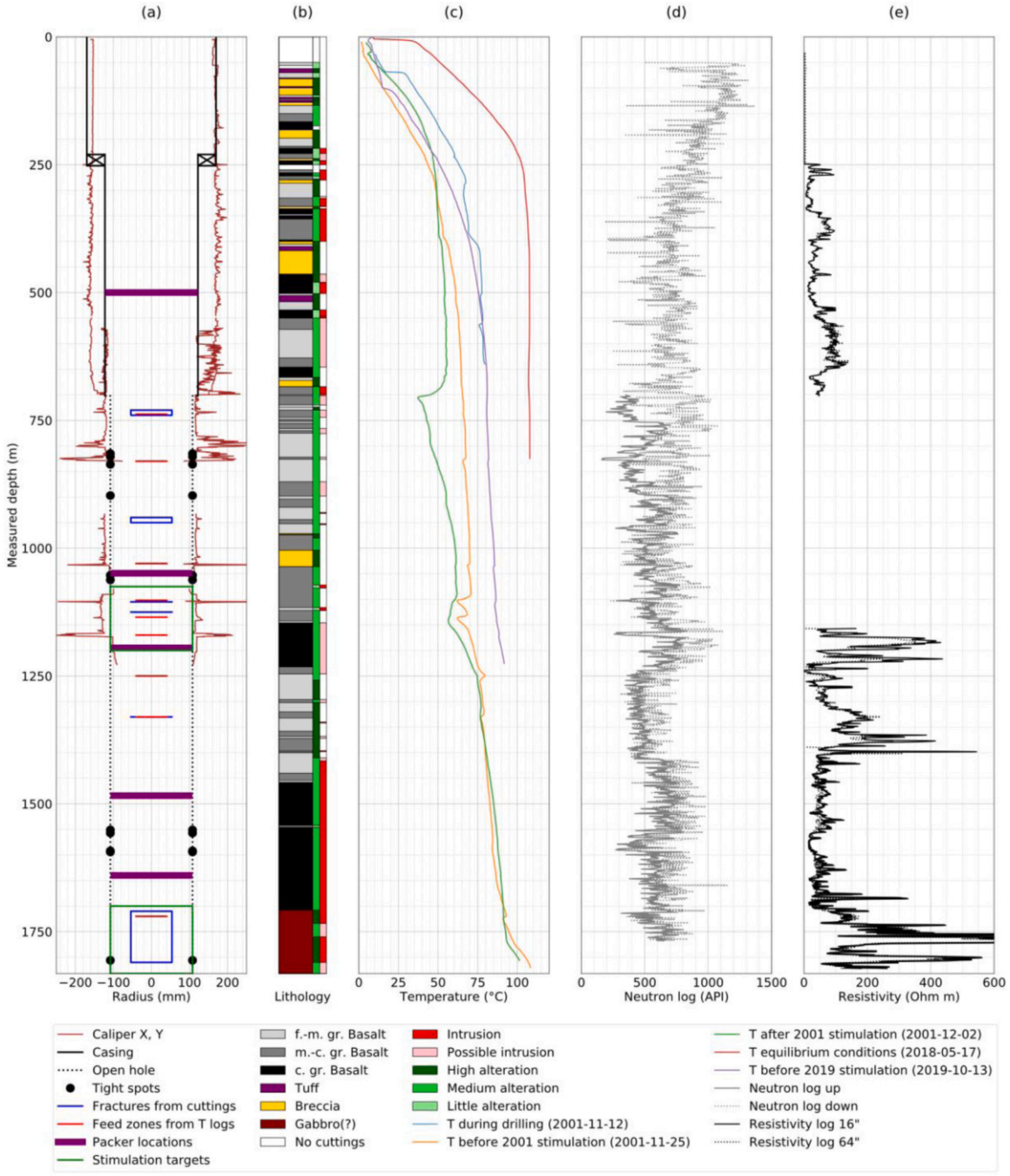

Fig. 5. (a) Completion and caliper logs of well RV-43. Fracture zones inferred by Richter et al. (2001) from cuttings and temperature logs and tight spots during initial reaming operations on 11 October 2019 are displayed. These are the stimulation targets. Additionally, packer locations during the four stimulation stages are shown. (b) Lithological profile of the well. (c) Temperture logs before the 2019 stimulation. (d) Neutron logs and (e) resistivity logs that were used to constrain the packer locations where no caliper log was available.

temperature logs run after drilling. From cuttings analysis, it was obvious that some mostly impermeable fractures filled with secondary minerals were intersected. These fractures were located at ~730–740 m, ~940–950 m, ~1105 m, ~1125 m, ~1330 m, and ~1710–1810 m MD (Fig. 5a).

After drilling an air lift test was performed, where the well started flowing at 1.9 MPa with flow rates of ~2–3 l/s. Temperature logs from that time show a major inflow zone at ~1100 m MD (Fig. 5c). To increase the productivity the well was hydraulically stimulated for ~3 days with flow rates between 40 and 60 l/s and WHPs of 6.6 to 10 MPa. An airlift test after the stimulation showed an increase of production rates from ~2–3 l/s to ~7–8 l/s (fold of increase FOI = 2.3–4.0) at similar pressure drawdown. Temperature logging performed after pumping revealed that most of the water had flown through feed zones just below the end of the casing at 702 m MD, and only a small fraction of the injected water had reached a feed zone at ~1250 m MD (Fig. 5c). No water had reached the deeper parts of the well. These operations are summarized in the drilling report by Richter et al. (2001).

A new borehole televiewer (BHTV) log was run on 13 to 14 October 2019 at 938 - 1029 m MD before the first stimulation stage (Figure S2; Table S1; Text S1). The most pronounced fractures within the logged interval strike NE-SW (partially open) and ENE-WSW with dip angles of

>60° from horizontal (Fig. 6).

3. Stimulation and monitoring methods

3.1. Stimulation targets

The primary goal of the stimulation is a further productivity increase in addition to the productivity increase from ~1.4 l/s/MPa to ~3.9 l/s/MPa achieved by the hydraulic stimulation performed after drilling in 2001. A further fold of increase (FOI) by ~2–3 with a minimum productivity index (PI) of ~10 l/s/MPa is the target of the 2019 stimulation. This goal is to be achieved by isolating and stimulating existing fracture zones separately through a straddle packer assembly.

The target sections are pre-fractured zones marked in green in Fig. 5a. This includes the fracture zone between 1100 and 1150 m MD and the intersection of the gabbro body below 1700 m MD. We intend to stimulate the two pre-existing fracture sets (striking ~N5°E and ~N40–50°E), which are assumed to be nearly vertical and at an angle of ~15–22° to the wellbore azimuth, below the fracturing pressure, i.e. by hydro-shearing. Given the possible fracture and SHmax orientations it is likely that the well intersects near critically stressed fractures. Thus, limited overpressures would be sufficient to hydraulically stimulate the well.

Secondary goals are the comparison of different injection schemes in terms of hydraulic performance increase and seismicity; and the demonstration of seismic risk assessment and mitigation procedures such as an adaptive traffic light system, zonal isolation and the cyclic soft stimulation concept. Field operations for the hydraulic stimulations performed in well RV-43 lasted from 11 October until 2 November 2019. A timeline of all field operations including wellbore measurements before and after the stimulations is provided in Table 1.

3.2. Zonal isolation

Zonal isolation was required since the open hole section has already been primary stimulated. The new treatment intends to stimulate additional smaller feed zones and the major feed zone along the 8 1/2'' open hole. The new stimulation intervals were identified based on existing information acquired from temperature logs and lithological profiles. Setting depths for the inflatable packers, and space out intervals for the straddle assembly and positions of the stimulation sleeves were adjusted based on old and new well log information. In addition to standard well logs, a borehole televiewer (BHTV) log (Fig. S2; Table S1; Text S1) and a borehole camera (Fig. S3) were run. Primary target intervals are shown in Fig. 5a. Fractured and highly altered basalts with high and variable resistivity, low neutron API and increased caliper were chosen as injection intervals while unaltered and intact doleritic intrusions with homogeneous and in-gage caliper, low and homogeneous resistivity, and high neutron API were chosen to set the packers.

A single ball set straddle packer assembly with inflation line between top and bottom packer was used for zonal isolation of Stage 1. All other stages were sealed off by using the top packer only and not inflating the bottom packer to target multiple fracture zones simultaneously.

The hydraulic straddle (or single packer) assembly was positioned in the open hole section and activated with a ball-drop inflation mechanism. Once the inflatable packers were positioned, set and tested, fresh water was pumped through the 4–1/2'' E75 16.6 lb/ft drill pipe and the stimulation sleeves. After pumping fresh water and flow back, the ball drop deflation system was activated to pull the straddle assembly out of hole. This procedure was performed for each stage (Stage 1: packers at 1049 and 1195 m, Stage 2: packer at 1484 m, Stage 3: packer at 1640 m, Stage 4: packer at 500 m).

3.3. Injection schemes

Well RV-43 was successfully stimulated in 2001 at ~702 m MD with maximum wellhead pressures of ~10 MPa and maximum injection rates of ~60 l/s. Similar values were targeted for the stimulation in 2019. However, injection parameters are not only constrained by geological boundary conditions, but also by available technical equipment. In particular, the maximum stand pipe pressure of the rig was 20.7 MPa. To reach the required injection flow rates two mud pumps and one high pressure cementing unit were run in parallel. Each pump supplied a minimum flow rate of 9–15 l/s and a maximum flow rate of 18.1–29.3 l/s depending on the pump liner size. The maximum flow rate of the available water supply was <60 l/s. The injection water was sourced

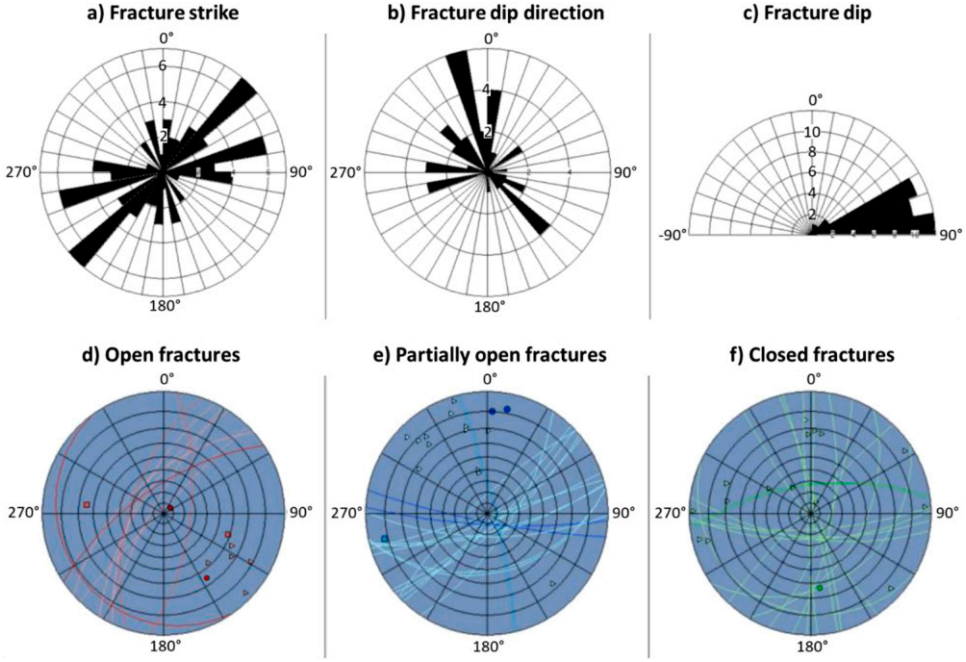

Fig. 6. Strike (a), dip direction (b) and dip (c) of all fractures identified from the acoustic borehole imager log shown in Figure S2 and orientations of open (d), partially open (e) and closed/filled (f) fractures shown on Wulff plots.

Table 1
Timeline of major field operations (RIH = run in hole, POOH = pull out of hole).

Time	Operation	Depth (m)	Comments
17.05.2019	Borehole camera	0 – 830	Obstruction at 830 m
11.10. 03:15	Reaming	0 – 1832	
12.10. 23:30	Temperature log	0 – 850	Stopped at 835 m and 850 m
13.10. 03:00	RIH casing	0 – 933	To overcome obstructions
13.10. 13:45	Temperature log	0 – 1225	
	Caliper log	913 – 1054	
	BHTV log	938 – 1029	
14.10. 00:00	RIH casing	933 – 1088	To overcome obstructions
14.10. 02:45	Caliper log	1089 – 1228	
14.10. 06:00	POOH casing	1088 – 0	
14.10. 18:30	Stage 1 prep + RIH	0 – 1197	
15.10. 23:45	**Stage 1 stimulation**		Crossflow
21.10. 14:30	Stage 1 prep + POOH		
22.10. 06:00	Stage 2 prep + RIH	0 – 1186	Obstruction at 1186 m
22.10. 19:00	Stage 2 POOH	1186 – 0	
23.10. 01:30	Reaming	0 – 1832	
24.10. 07:30	Stage 2 prep + RIH	0 – 1789	10 hrs stop due to weather
25.10. 04:45	Temperature log	0 – 1770	Logging through drill pipe
	Neutron + gamma log	50 – 1770	
25.10. 14:45	POOH	1789 – 1484	
25.10. 19:00	**Stage 2 stimulation**		Crossflow
26.10. 00:00	Stage 2 prep + POOH	1484 – 0	
26.10. 09:45	Stage 3 prep + RIH	0 – 1646	
27.10. 00:00	**Stage 3 stimulation**		Sealing after crossflow
29.10. 00:00	Stage 3 flowback		
29.10. 14:30	Stage 3 prep + POOH	1646 – 0	
30.10. 00:30	RIH liner	0 - 1598	Obstruction at 1598 m
30.10. 19:30	POOH liner	1598 - 0	
31.10. 07:00	Stage 4 prep + RIH	0 – 500	
31.10. 11:15	Casing integrity test		
31.10. 12:50	**Stage 4 stimulation**	500 – 1832	Sealing; Integrity test & Stim.
01.11. 01:00	Stage 4 prep + POOH	500 – 0	
01.11. 05:00	Reaming	0 - 1791	
02.11. 03:00	RIH liner	0 - 1773	
08.11.2019	Temperature log	0 – 1769	

from the water network of the city. To keep the water supply during the stimulation job continuous and to allow short cycles with higher flow rates, a water storage tank of 100 m^3 capacity was available at the site.

An exemplary injection design for one stage is shown in Fig. 7. First, the fracture opening pressure (FOP) is approached slowly and determined by increasing the flow rate stepwise with cyclic flow rate reductions. Once the FOP is known the last injection cycle is repeated multiple times. This is followed by cyclic pulse injection where the injection volumes are the same as in the cyclic injection before. Afterwards, the same volume is injected again with constant flow rate. A repetition of this procedure allows comparing the seismic and hydraulic response of the reservoir to the different injection schemes. In the end the flow rates and pressures are reduced stepwise and part of the injected water is produced back before the next stage is going to be stimulated. This injection schedule was the base for each injection stage and had to be adapted based on the observations during each stage.

3.4. Seismic risk assessment

A pre-stimulation seismic hazard and risk assessment was performed by Broccardo et al. (2020). It was based on a fully probabilistic framework, including epistemic and aleatoric variability, different earthquake rate models (both statistical; Mignan et al., 2017, and physics-based; Karvounis et al., 2014; Karvounis and Jenny, 2016), a set of the ground motion characteristic models, a selection of vulnerability functions and the related consequence models (e.g. Mignan et al., 2015). Two risk metrics together with two risk thresholds were selected for pre-stimulation decision making. The first risk metric was the individual risk (IR) with a threshold of 10^{-6}, and the second was a low damage metric with a threshold of 10^{-2}. The individual risk is defined as the annual frequency at which a statistically average individual is expected to experience death or a given level of injury from the realization of a given hazard (Broccardo et al., 2017a; Mignan et al., 2019a,b). The second risk metric is the damage risk. Damage risk is defined as the frequency over the time span of the project at which a statistically average building class is expected to experience light non-structural damage from the realization of a given hazard.

The results of the risk assessment by Broccardo et al. (2020) indicate that the overall risk for an individual to die in a building within a radius of 2 km around the well is below 10^{-7}. This value is well within the acceptable range when compared to acceptance criteria applied in other European countries like in the Netherlands or Switzerland (van Elk et al., 2017). The reasons for the acceptable risk are the estimated low vulnerability of the building stock, the overall limited injection volume and the constraints posed by the 2001 injection data. The chance of

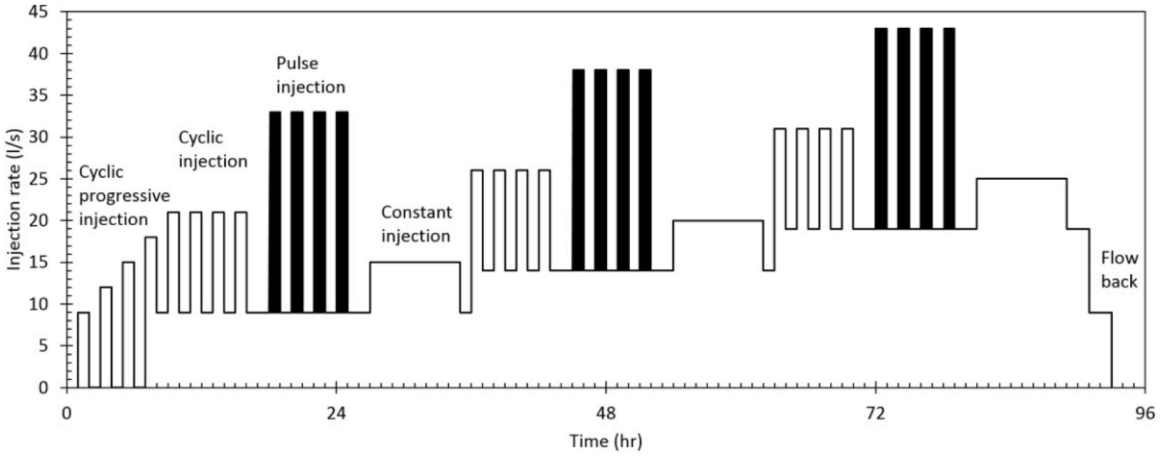

Fig. 7. Exemplary injection scheme with assumed initial fracture opening at 15 l/s. The same cyclic, pulse and constant injection scheme is repeated three times with the same volume being injected during each scheme. Flow rates are increased during the stimulation to achieve the required stimulation pressures depending on the increasing injectivity of the system.

damage to buildings is around 0.1% and therewith well below the 10^{-2} acceptance threshold. Moreover, the thresholds proposed in the classical traffic light system (Fig. 8) are consistent with the risk thresholds computed. Finally, the uncertainties at the initial stage of the project were very high (mostly due to uncertainty on underground seismic feedback to injection; e.g. Mignan et al., 2019b), highlighting the importance of updating the risk study continuously as new data become available (Broccardo et al., 2017b). This was done here through the application of an Adaptive Traffic Light System (ATLS, Trutnevyete and Wiemer, 2017; Kiraly-Proag, et al., 2016, 2018).

3.5. Seismic risk mitigation

State of the art seismic risk mitigation should not only rely on a single measure but consist of a number of interconnected layers that each will add to an as safe as reasonably possible project execution. Below we describe the different safety measures we applied.

3.5.1. Cyclic injection

It has been proposed based on several past experiments at multiple spatial scales that cyclic injection at different temporal scales (short term cycles = seconds to minutes, medium term cycles = minutes to hours, long term cycles = hours to days) leads to lower magnitudes of seismic events, lower breakdown pressures and more complex fracture systems (Hofmann et al., 2018b). This is attributed to hydraulic fatigue resulting from pulse pressurization (short term cycles; Zang et al., 2013), stepwise stimulation (medium-long term cycles), and stress relaxation and seismicity decay in between high rate injection phases (Hofmann et al., 2018a; Kwiatek et al., 2019; Zang et al., 2019). The overall goal of cyclic injection is a more controlled fracture development to increase permeability with reduced seismic risk. However, so far, no accepted procedure exists on how long individual cycles should last. To compare different fluid injection schemes, it was planned to apply continuous, cyclic (one hour high injection rate followed by one hour low injection rate), and cyclic pulse (same as cyclic, but with three minutes high injection rate followed by three minutes low injection rate during the one hour high injection rate phase) injection treatments subsequently within each stage (Fig. 7).

3.5.2. Multi-stage injection

The application of a multi-stage injection serves several purposes. First, the stimulation of specific intervals along the open hole section is only possible by sealing off the well above and below the stimulation target zone. In the RV-43 well, this is mandatory as the entire open hole section has already been stimulated in 2001. Second, the stimulation of multiple sections potentially leads to a higher overall productivity increase as compared to the stimulation of only one section since multiple new inflow zones are developed. Third, the seismic risk is expected to be reduced compared to a massive open hole or single-stage stimulation. This is because only smaller individual volumes are stimulated in each stage as compared to one large volume (Meier et al., 2015).

3.5.3. Slow flow rate changes, limited injection rates and flow back instead of shut-in

At the start of the treatment, flow rates are increased stepwise. This allows to determine the fracture opening pressure and to slowly approach critical pressures needed for stimulation and inducing seismicity. Once the fracture opening pressure is known, the flow rates are not increased significantly anymore. At the end of the treatment the flow rates are reduced slowly to avoid abrupt changes of pressures and stresses in the reservoir and part of the injected fluid is flowed back. The flow back has been proposed as an effective risk mitigation strategy, because it was observed that the magnitude of induced seismic events may increase during shut-in periods after the stimulation (e.g. Basel, Mukuhira et al., 2017). On the other hand, it was demonstrated that flow back instead of shut-in can lead to an immediate reduction in earthquake activity during the flow back period (e.g. Pohang, Hofmann et al., 2019).

3.5.4. Monitoring of fluid volumes

It is a well-established fact that on average the maximum observed magnitude of induced earthquakes scales with injected volume, although there is no final agreement if this empirical observation is largely a statistical effect (Gischig and Wiemer 2013; van der Elst et al., 2016) or a physics-based boundary (McGarr, 2014). At several Enhanced Geothermal System (EGS) projects, a site-specific seismic magnitude – injection volume relationship has been observed and it can be used to steer the injection strategy. For example, at one of the stimulations of the Pohang EGS this relationship, and the deviation from it, were used to constrain the maximum fluid injection volume before the stimulation to stay below a predetermined target magnitude during injection (H. Hofmann et al., 2018a; 2019). This approach was also applied for real-time analysis at the Helsinki EGS project (Kwiatek et al., 2019). During the stimulation of well RV-43, injected net volumes, and seismic moment magnitudes were observed and related to each other in a similar fashion in order to be able to observe critical trends that would suggest to stop injection before indicated by the traffic light systems.

3.5.5. Classical seismic traffic light system

Seismic traffic light systems (TLS) are standard procedures to manage seismic risks for fluid injection activities. In Iceland it is applied for example for re-injection activities in the Hellisheidi geothermal field (Thorsteinsson and Gunnarsson, 2014). For the Geldinganes project, the

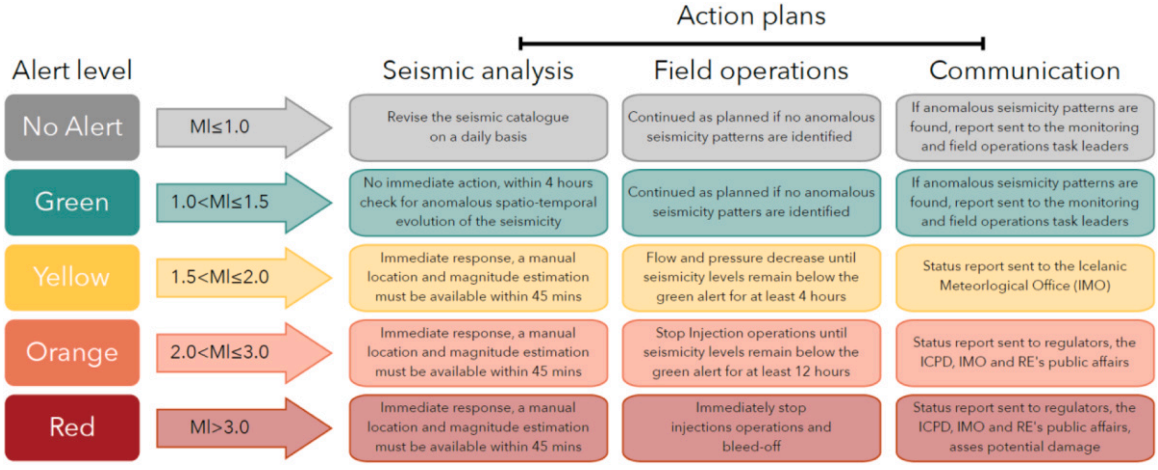

Fig. 8. Primary traffic light system (TLS) for the hydraulic stimulation of well RV-43 in October 2019 (modified from Broccardo et al., 2020).

pre-defined TLS agreed between operator and regulator is shown in Fig. 8. We use a communication protocol that is similar to the one used in the TLS of the Hellisheidi geothermal field, while for Geldinganes, magnitude levels, seismic protocols and field operations protocols have been specifically designed for this application. Depending on the local magnitude of induced seismic events the flow rates are adapted according to this traffic light system. The TLS may be summarized as follows: Below Ml 1.5 the stimulation may continue as planned if no anomalous seismicity patterns are identified. Above Ml 1.5 flow rates and pressures are reduced until seismicity levels remain below the green alert for at least 4 h. Above Ml 2.0 injection is stopped and the well is opened for flow back until seismicity level remains below the green alert for at least 12 h. Ml 3.0 is the target magnitude that should be avoided by applying this TLS. If a red traffic light alert is reached, the well will be flowed back as long as possible and injection at the site will not resume again without an additional risk study. In addition to the conventional TLS, an adaptive TLS was applied for the first time in the field. The more conservative of the two served as the decision criterion. More information on the TLS protocol is provided in Text S2.

3.5.6. Adaptive traffic light system

The proposed adaptive traffic light system (ATLS) is based on the work of Mignan et al. (2017). ATLS is data driven and intends to overcome the limitations of the traditional heuristic methods. It integrates all risk-relevant information available in near real-time, including the future injection plan, and computes a probabilistic, time-dependent risk assessment. In the ATLS the assignment of a magnitude threshold is dynamic and based on a quantitative risk assessment, subject to a safety criterion imposed by the authorities (in this project individual risk $IR<10^{-6}$). As a consequence, the ATLS is an objective and more robust mitigation strategy, which facilitates a fair and transparent regulatory process. This approach is in line with the protocols common for most other technological risks, such as in the hydropower, nuclear or chemical industries.

The ATLS is a continuous, automated update of the a-priori risk assessment. Here we update only one of the branches of the a-priori risk study published by Broccardo et al. (2020), the S1 model, that assumes a linear relationship between seismicity rate and flow rate, as well as an exponential decay term for post-injection rate (see Mignan et al., 2019a, b). The model is fully integrable yielding a closed-form ATLS solution and depends only on three physically meaningful parameters that are updated as new data becomes available during stimulation. The detailed method and results of the ATLS updating strategy will be summarised in a separate publication, here we report only on the overall results.

3.6. Seismic monitoring and data analysis

The recent seismic activity near Reykjavik is low and little is known about larger historical events. Also, the knowledge about weak seismic events with $M<1$ is limited, due to the lack of a dedicated network. In the framework of fluid injection operations and geothermal stimulation, monitoring the migration of induced (micro-) seismicity requires precise hypocentral location and robust magnitude estimation in real-time (Grigoli et al., 2017). The detailed analysis of induced microseismicity in space and time as well as studies of the source parameters of small earthquakes allow to track the spatial distribution of fractures within the reservoir. It can help to identify active faults and lineaments that may trigger large induced seismic events as well as to optimize hydraulic stimulation operations and to locate the regions with higher permeability, enhancing energy production.

In late 2018 Iceland Geosurvey (ISOR) and Reykjavik Energy (OR) set up a local monitoring network with 5 short period (1 Hz) seismic stations and instrumented 1 shallow borehole site (stations 1–6 in Table 2; network code YG, internal name Veitur "VE"). To enhance the detection of signals from weak earthquakes, we complemented the dense Geldinganes network by a small aperture surface array (7 stations on Geldinganes, marked as station 7 in the Table 2 and Fig. 1), additional short period seismic stations (stations 8–13) and borehole geophones (station 14, Fig. 1 and Table 2). The temporary instruments were provided by the GIPP instrument pool of GFZ Potsdam and were removed in November 2019. The borehole geophone chain was not in operation anymore during the stimulation due to technical failure.

Table 2
Seismic Stations installed as permanent and temporary stations in the frame of the DESTRESS project (Abbreviations: Short Period = SP, *A* = Array, 3-component = 3c). Stations 1–12 transmitted data in near real-time to the analysis center at ISOR. Data from the island Lundey (13) northwest of the stimulation site were integrated during the post-processing. The 17-level geophone chain (14) was not in operation during the stimulation due to technical failure.

ID	Network code	Frequency	Installation	Description
1	VE.Veitur	SP, 200 Hz	Buried	Surface station, 1 Hz, 3c
2	VE.Skoli	SP, 200 Hz	Buried	Surface station, 1 Hz, 3c
3	VE.Geldv	SP, 250 Hz	Borehole	122.5 m, 1 Hz, 3c
4	VE.Gelda	SP, 200 Hz	Buried	Surface station, 1 Hz, 3c
5	VE.Brim	SP, 200 Hz	Buried	Surface station, 1 Hz, 3c
6	VE.Nidur	SP, 200 Hz	Buried	Surface station, 1 Hz, 3c
7	YG.GA1.. GA7	A, SP, 200Hz	protected	Surface stations, 7 stations, 1 Hz, 3c
8	YG.Geldw	SP, 200 Hz	buried	Surface station, 1 Hz, 3c
9	YG.Gelde	SP, 200 Hz	protected	Surface station, 1 Hz, 3c
10	YG.Blika	SP, 200 Hz	protected	Surface station, 1 Hz, 3c
11	YG.Esja	SP, 200 Hz	protected	Surface station, 1 Hz, 3c
12	YG.Lykk	SP, 200 Hz	Borehole	25 m, 4.5 Hz, 3c
13	YG.Lund	SP, 200 Hz	protected	Surface station, 1 Hz, 3c Station on island Lundey
14	YG.R42	SP, 2000 Hz	Borehole	Borehole geophone chain, 1040–1200 m, 17 geophones, 15 Hz, 3c

Most of the surface stations were set-up on hard rock, minimizing local effects and noise amplification due to shallow soft layers. The surface stations were either placed in a barrel buried in the ground, filled partly with concrete coupled to the hard rock or under a protective bucket covered with sand and stones which shield against direct wind contact. The stations were in a distance range from 1 to 7 km from the stimulation area. Besides the stations listed above, data from another seismological network in the Hengill region, ~20 km to the east, was integrated for an improved analysis. Using the Bayesian Magnitude of Completeness (BMC) method (Mignan et al., 2011) calibrated to Icelandic conditions (Panzera et al., 2017), we estimated a completeness magnitude of Mc~0. In the unlikely case of an earthquake with magnitude above the TLS limit, most of the seismic stations (velocity sensors) of the Geldinganes network would be saturated and would have been useless for location and magnitude estimation, thus it was important to have access to a few IMO stations outside of the Geldinganes area as well.

The main duties of the routine seismologist were:

1) Respond to the alerts following the instruction in the TLS
2) Manually locate the events and keep the catalog clean (remove false events). Estimate the local magnitude by excluding the stations within 3 km from the epicenter. For event above Magnitude 2 use the same stations as the Icelandic Meteorological office (IMO) if available.
3) Check for anomalous seismic activity that might have an impact on the safety of the operations (e.g. lineaments/faults identification) and report to the internal expert panel and field operations task leaders.

3.6.1. Automatic real-time analysis

All waveform raw data were transmitted with LTE communication to

the main data center at Iceland GeoSurvey (ISOR, http://en.isor.is/) allowing for near real-time analysis for event detection, event location, magnitude evaluation as well as automatic event notification and alerting via SMS and email within seconds after an event has occurred. The automatic event detection, event location and magnitude determination were done with a SeisComp3 system (SC3, https://www.seiscomp3.org/). For event detection we used scanloc (Grigoli et al., 2018b), the SC3 module for local seismicity monitoring, which, in combination with the scautopick extension S-AIC that provides automatic accurate S-picks, produces more reliable detection and location results. For location refinement we used screloc, the SC3 module based on the NonLinLoc (Lomax et al., 2000) algorithm which allows to further improve the location results. This fast automatic event solution provided an absolute location accuracy of less than 300 m.

We tested different seismic velocity models to minimize the location and source mechanism errors for the Geldinganes area. The starting seismic velocity model was based on seismic refraction profiles in the vicinity of Geldinganes (Flóvenz, 1979) and a refraction profile north of the area (Bjarnason et al., 1993). One refraction profile is just south of Geldinganes, but Geldinganes and the area north of it are in the roots of a volcanic complex with gabbroic intrusions, so the velocity is expected to be higher there (Tryggvason et al., 2002).

Maps and graphs of the induced seismic activity were produced and updated simultaneously by ISOR, ETH and GFZ which were needed as background information for the stimulation team and the TLS. The time from July 2019 until the stimulation phase was used to improve the velocity model as well as the parameters for the local magnitude ML calculation. In addition, an explosion NW of the stimulation site was used to check the velocity model, the sensor orientation of the horizontal components and the seismic station settings (amplification, meta-data).

3.6.2. Semiautomatic analysis in near real-time

To improve the automatic location accuracy and to extract more details about the source mechanism, a series of secondary semi-automatic processing stages were triggered by SC3 when an earthquake was detected. These included the enhanced detection by waveform stacking methods (based on LASSIE in the Pyrocko python toolbox, Heimann et al., 2017), relative earthquake location (such as HypoDD; Waldhauser and Ellsworth 2000), and a probabilistic moment tensor inversion for the larger events (using Grond, Heimann et al., 2018; Kühn et al., 2020). The improved location accuracy was <100 m. More details on the inversion technique and the waveform processing are provided in Text S3 and Table S2.

3.7. Hydraulic monitoring and data analysis

During the hydraulic stimulation of well RV-43 pure water from the water supply of the city was injected through the drill string without additives. The injection rate was calculated from the pump strokes for the different liner sizes. Injection pressure (stand pipe pressure) and annulus pressure were measured at the surface in real-time while three downhole memory tools measured pressure and temperature above and below the bottom packer and above the top packer. Flowback rate through the drill string was measured by a flowmeter. Annulus flow, which occurs with crossflow around the packer, was measured manually at specific points in time.

The hydraulic performance indicators were calculated based on the injection rate q (m^3/s) and the overpressure Δp (Pa) in the injection interval measured by the memory tool above the bottom packer (straddle packer assembly) or below the top packer (single packer assembly). This overpressure is the measured pressure p (Pa) minus the initial reservoir pressure p_0 (Pa). The injectivity index II ($m^3/s/Pa$) is defined by Eq. (1):

$$II = \frac{q}{p - p_0} = \frac{q}{\Delta p} \tag{1}$$

The injectivity increase is defined as folds of increase FOI (-), which is the injectivity index after a specific operation (II_{after}) divided by the injectivity index before this operation (II_{before}).

Pressure fall-off periods during shut-in were additionally analyzed using conventional well test analysis as described in Hofmann et al. (2019). This allows to calculate the transmissivity kh (m^3), well skin s (-), compressibility c (m^3/Pa) and the theoretical productivity index PI ($m^3/s/Pa$) of the well for pseudo steady-state conditions.

The fall-off sequences (shut-in periods) during the stimulation treatments were analyzed using classical well test analysis (e.g. Horne, 1995). The evolution of transmissivity and permeability is thus calculated from pressure decline curves after each injection stage, taking into account the superposition principle and assuming infinite-acting radial flow. The calculations are based on the generalized formula for pressure p (Pa) development with stepwise flow rate q (m^3/s) changes (e.g. Lee, 1982):

$$p(r,t) = p_0 + \sum_{i=1}^{n} \frac{(q_i - q_{i-1})\mu}{4\ \pi\ k\ h} \left(\gamma + ln\left(\frac{\Phi \mu c_t r^2}{4k(t - t_{i-1})} \right) - 2s \right) \tag{2}$$

where r (m) is the well radius, p_0 (Pa) is the initial pressure, c_t (m^3/Pa) is the total compressibility, s (-) is the skin, t (s) is the total time, t_i (s) is the interval time, h (m) is the interval length, q_i (m^3/s) is the interval flow rate, k (m^2) is the permeability, μ (Pas) is the dynamic fluid viscosity, Φ (-) is the porosity and γ=0.5772 is the Euler constant. The transmissivity kh (m^3) is calculated from the logarithmic superposition time derivative of the pressure decline curve after Lee (1982):

$$\frac{\partial(\Delta p)}{\partial\left(\ln\left(\frac{t_s}{t_s + t_{inj}} \right) \right)} = \frac{q\ \mu}{4\ \pi\ k\ h} \tag{3}$$

where t_s (s) is the duration of the fall-off (shut-in) time and t_{inj} (s) is the total injection time.

The productivity index PI ($m^3/s/Pa$) is calculated according to the pseudo steady-state solution of Lee (1982):

$$PI = \frac{q}{\Delta p} = \frac{2\pi kh}{\mu} \frac{1}{\ln\left(\frac{R}{r} \right) - 0.75 + s} \tag{4}$$

where R (m) is the radius of the reservoir (as no flow boundary).

3.8. Chemical monitoring and data analysis

Flowback water from the drill string was analyzed continuously for chemo-physical parameters by temperature-resistant electrodes (dissolved oxygen (DO), pH-value, electric conductivity (EC), and redox potential (Eh)) installed in a flow-through cell equipped with data logging and storage unit "Liquiline". In addition, discrete water samples were collected at certain time intervals. In a subsample H_2S and silica (SiO_2) were measured photometrically and bicarbonate was measured by titration immediately after sample collection. Metals (Si, Al, B, Fe, K, Mg, Ca, Mn, Na) were analysed in filtered (0.45 μm) and acidified samples (acidification in field by HCl to pH < 2) by inductively coupled plasma optical emission spectroscopy (ICP-OES) and anions (sulfate, chloride, fluoride) shortly after filtration (0.45 μm) by ion chromatography.

Isotopes of water (^2H, ^{18}O, ^{17}O) were analyzed by thermal ionization mass spectrometry (TIMS) using a Picarro L-2140i ring-down spectrometer with an external precision of ± 0.0005 as determined by repeated analyses of the international standard NBS 987. Each sample was injected ten times and the last seven injections were used to calculate a mean value for δ^2H, $\delta^{18}O$ and $\delta^{17}O$ as well as the standard deviation. All samples were transferred to VSMOW scale using a two-point calibration with VSMOW2 and SLAP2 standard water derived from the International Atomic Energy Agency (IAEA). Besides the

flowback also three samples of the injected water were analyzed for cations, anions, and water isotopes.

4. Results

4.1. Stage 1: packers at 1049–1195 m

In the first injection stage the straddle packer assembly was set with the bottom packer at 1195 m and the top packer at 1049 m (Fig. 9a) to isolate the uppermost target zone (Fig. 5a). This stage was stimulated first since it was the only one with caliper information for packer placement. A total of 14,866 m^3 of water were injected on 16 – 21 October 2019 (Fig. 9f). The injectivity increased from below 4.0 l/s/MPa at overpressures <1.8 MPa and injection rates <9 l/s at the start of injection to ~16 l/s/MPa (FOI = 4) at the maximum flow rates of ~70 l/s and overpressures of 4.6 MPa. During the step rate increase the shut-in periods show a calculated productivity increase from 0.7 l/s/MPa to 7.5 l/s/MPa (FOI = 10.7) while the injectivity increased from 3.0 l/s/MPa to 12.0 l/s/MPa (FOI = 4). The final injectivity at the end of the treatment was 12 l/s/MPa (FOI = 3) during the lowest rate of ~20 l/s and overpressure of ~1.7 MPa (Fig. 9g). Seismicity was not detected during Stage 1.

Right from the start water was flowing from the annulus indicating that the top packer was not sealing (Fig. 9a). At this point the annulus was closed with the intention to stimulate the interval between the casing shoe at 702 m and the bottom packer at 1195 m. However, almost equal pressures and temperatures (Fig. 9d and e) above and below the bottom packer show that the bottom packer was also not sealing (Fig. 9d). In addition to the anticipated inflow zones between the packers and below the casing, a temperature log run on 25 October 2019 through the drill string revealed a third inflow zone in the cased section of the well between ~230 and 400 m (Fig. 9b). The leak occurred in a

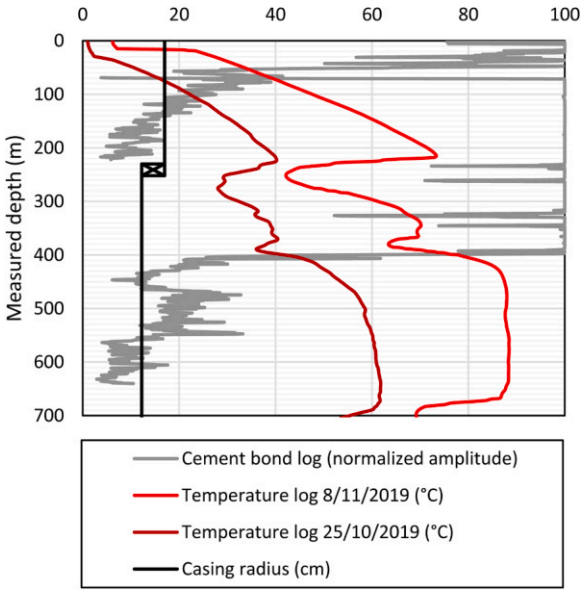

Fig. 10. Temperature logs, cement bond logs and casing scheme showing cold water infiltration in the uncemented interval between 230 and 400 m MD.

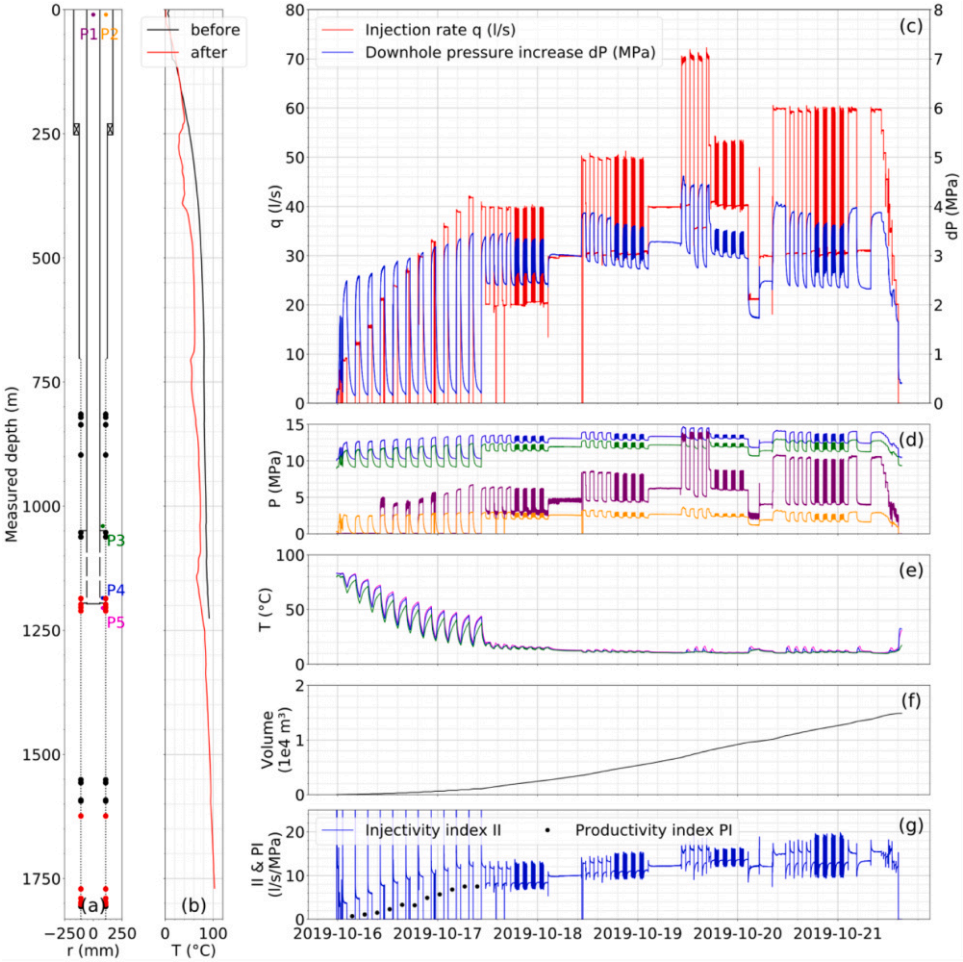

Fig. 9. Summary of injection Stage 1 with packers at 1049 and 1195 m. (a) Well schematic, monitoring points and tight spots during reaming before (11 October 2019; black dots) and after (23 October 2019; red dots) this stage, (b) temperature profile before (13 October 2019; black) and after (25 October 2019; red) this stage, (c) injection rate q and downhole pressure increase dP above the initial reservoir pressure measured above the bottom packer, (d) all pressures measured at the monitoring points P1-P5 (note that P4 and P5 are almost identical and overlap each other), (e) the fluid temperatures measured downhole, (f) the cumulative injected volume, and (g) the injectivity and productivity index based on the analysis of the fall-off curves during shut-in periods.

non-cemented part of the well at the point where the production liner is attached to the production casing (Fig. 10).

Despite the lack of seismicity, the real-time update of the ATLS was possible. Fig. 11 illustrates how the Individual risk (IR) evolved with time during the injection: At the end of day 4 (vertical line in Fig. 11), the a-priori IR of 10^{-8} (a factor of 100 below the acceptance threshold; see Broccardo et al., 2020) was reduced in the posterior by about a factor of 100 to 10^{-10}. During the subsequent stages the Individual risk remained at a similar level and is thus not shown.

4.2. Stage 2: Packer at 1484 m

In Stage 2 a single packer was set at 1484 m. This location was chosen based on the resistivity log, neutron log and lithological well profile. The stimulation target was the gabbro body at the bottom of the well. After an initial pressure increase to ~2.7 MPa at 5 l/s injection rate (II = 1.9 l/s/MPa) the pressure dropped and return flow through the annulus started, indicating crossflow around the packer (Fig. 12c). Therefore, the annulus was closed again, and the injection rate was increased in steps up to 40 l/s with no significant difference between the pressures (Fig. 12d) and temperatures (Fig. 12e) above and below the packer. Similar to Stage 1 the hydraulic data are representative for the whole wellbore including casing leak. Injectivity of the whole well permanently increased to 12 l/s/MPa even at low overpressure of ~0.6–0.7 MPa and flow rate of ~9 l/s and is only slightly higher for larger overpressure of ~2.8 MPa and flow rate of ~40 l/s (Fig. 12g). Productivity determined from shut-in data at the end of Stage 2 was similar to the final injectivity of Stage 1 and the injectivity during the crossflow period of Stage 2. During Stage 2, where only 363 m^3 were injected (Fig. 12f), also no locally induced seismicity was registered.

4.3. Stage 3: Packer at 1640 m

In Stage 3 the packer was set at 1640 m. Similar to Stage 2 the packer location was chosen based on resistivity logs, neutron logs and well lithology. The target was again the gabbro body and the associated fracture zone below 1710 m MD. The results of Stage 3 are summarized in Fig. 13. After an initial pressure increase to ~3.2 MPa pressure also dropped in Stage 3 due to crossflow indicated by return flow from the annulus. This time, the annulus was left open, and injection was continued. This was done because the same pressure response as during the crossflow in Stage 2 was observed, where some differential pressure across the packer remained until the point when the annulus was closed (Fig. 12 at 20:10). Afterwards, there was no pressure difference anymore. To maintain a certain differential pressure the annulus was left open during the entire Stage 3. During most of the initial flow rate steps the pressure first increased and subsequently decreased. Return flow was significant, but not measured during that time due to operational reasons. During the ~30 l/s step the overpressure suddenly increased from ~4 MPa to ~9 MPa within ~15 min. At that time also the first cluster of seismic events was observed around the packer location (~1425 m TVD) with the largest moment magnitude of Mw = −0.01 (Fig. 13 and Fig. 14). From that point on the return rate from the annulus was measured periodically. About 8.5 h after start of injection the return rate completely ceased to zero accompanied by further pressure increase to >10 MPa. No significant further returns were observed for the rest of the treatment, likely due to plugging of the crossflow path as discussed in Section 5. The injectivity remained low and fairly constant between 2 l/s/MPa at 20 l/s and 3 l/s/MPa at 40 l/s. The calculated productivity from the shut-in phases however is significantly higher with 13–14 l/s/MPa. The reason for this difference is likely the overpressure created in a confined volume by the injection. In total 4731 m^3 of water were injected at this stage from which an unknown, but relatively small (<500 m^3), amount was returning through the annulus in the beginning.

The temperature log run after the treatment (Fig. 13b) as well as the induced seismicity (Figs. 14 and 15) clearly show that most of the fluid entered below the packer and stimulated the target zone. Most of the induced seismicity occurred at a short distance from the injection interval towards the north of the well in a small cluster (Figs. 14 and 15). With time, seismic events developed over a broader depth range from ~1 to 2 km. Most of the activity was located some hundred meters further south and west from the initial cluster.

In total 70 events with three and more picks were used for moment tensor inversion (Figs. 14 and 16). For 23 events stable solutions could be determined (Figs. 16 and 17). Magnitudes and locations were only determined for these stable solutions. Based on the cumulative focal

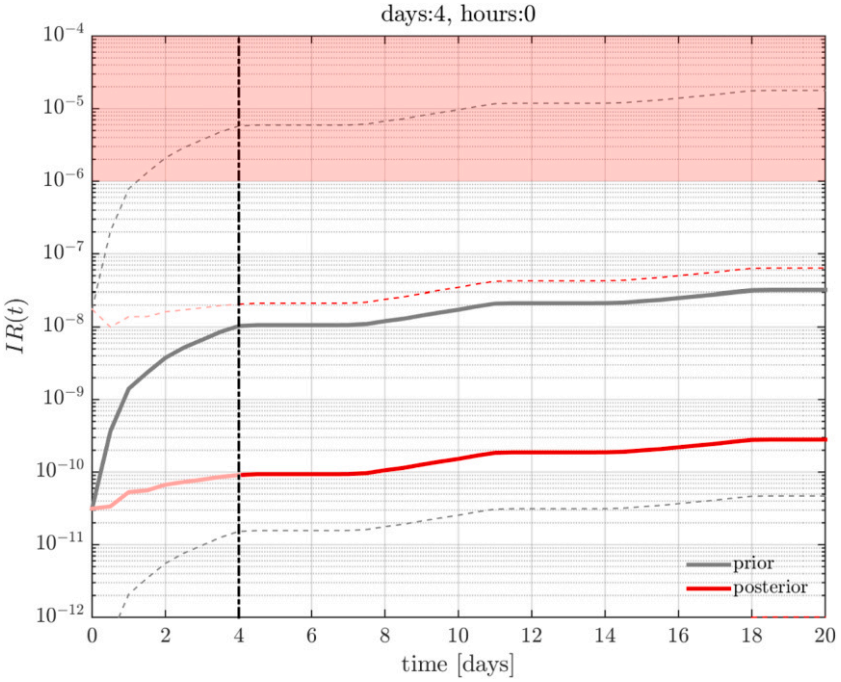

Fig. 11. Individual risk (IR) assessed before start of injection (prior) and after 4 days of injection (posterior).

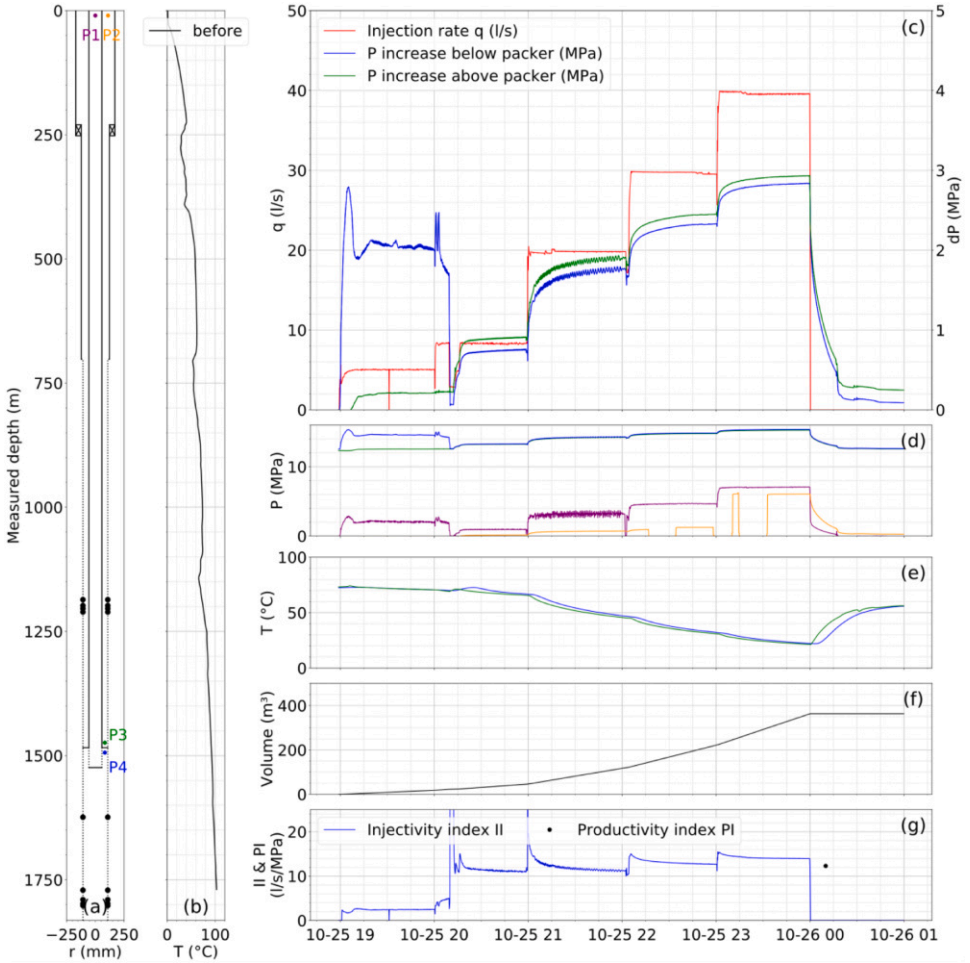

Fig. 12. Summary of injection Stage 2 with packer at 1484 m. (a) Well schematic, monitoring points and tight spots during reaming before the stage (23 October 2019; black dots), (b) temperature profile before (25 October 2019) this stage, (c) injection rate q and downhole pressure increase above the initial reservoir pressure measured above (P3) and below (P4) the packer, (d) all pressures measured at the monitoring points P1-P4, (e) the fluid temperatures measured downhole, (f) the cumulative injected volume, and (g) the injectivity and productivity index based on the analysis of the fall-off curves during shut-in periods.

mechanism, N18°W striking structures with a dip of 88° were activated with a rake of 177°. The subvertical seismic cloud including all 23 events is oriented ~N-S (largest events) to NE-SW (all events). Most stable solutions are close together. The first events are located north, and later events occur further south and possibly shallower and with a slightly different orientation. In the very end, two events occur about 400 m further NE. Most fault plane solutions indicate a strike-slip regime (Figs. 14 and 15) with a P-axis azimuth, an indication for the maximum stress direction, of ~N20°E for the initial cluster and between N20°E and N40°E for the later seismic activity. The NE to NNW oriented subvertical seismic cloud and the NE-SW oriented maximum horizontal stress direction refine the initial estimates of the stress field and structural geology.

The seismicity reached a maximum magnitude of about 0, which was well below the threshold of a yellow alert (Ml >=1.5, see Fig. 8). An Mw 0 earthquake in a medium with a shear modulus of 20 GPa and a slip area of 10 m x 10 m would be consistent with an average slip dislocation of about 0.5 mm.

After injection, the injection string was opened for flowback. During this ~14.5-hour period >533 m^3 water were produced at flow rates restricted by the operator to ~23 l/s. After 10 min of flowback, at an overpressure of ~9 MPa, the pressure suddenly increased because the 2″ stand pipe valve got clogged up by the packer inflation ball which was unintentionally pumped back to surface. After removal of this obstruction at 1:25 am pressure and return rate remained unstable until a smooth pressure decay started from ~3 MPa and the flowback rate was not restricted anymore. During pressure reduction and flowback seismic activity ceased and magnitudes were significantly lower as compared to the continuous injection phase before.

Chemical analyses of the flowback were performed to identify mixing of injected water with reservoir fluid and to determine if waters from different reservoirs flow into the well. The measured data of main and minor elements show a continuous change in the water composition as compared to the injected water (Fig. 18 and Table 3). With increasing volume of produced water, the temperature, pH, electric conductivity, as well as the concentrations of most elements (boron, hydrogen sulfide, sulfate, chloride, bicarbonate, potassium, sodium, silicium) increased. In contrast, Ca decreased and fluoride and iron fluctuated showing no clear trend over time.

The redox potential decreased initially (until 6:00 am) down to −300 mV and increased afterwards again up to - 200 mV. At the same time, also the oxygen content began to rise slowly. Low redox and oxygen indicate usually deep formation waters since all oxygen from air or surface near waters would be consumed at depth by chemical reduction processes.

The silica concentration usually correlates with temperature in siliceous aquifers and are therefore an indicator for deep formation waters. The real dissolved silica is measured as monomeric silica, which can differ from the total silica concentration that can be higher when silica is oversaturated but kinetically hindered to precipitate as quartz or amorphous silica. Silica measured both as monomer (photometrically) and as total silica (by ICP), was identical by both techniques indicating silica to occur as monomeric silica thus being undersaturated in the produced water. Silica increased from 10 to 73 mg/l over time in the samples, which is still undersaturated at given high temperatures (based on PhreeqC calculations). However, values were still rising in samples collected over time indicating that reservoir composition has not yet been fully reached.

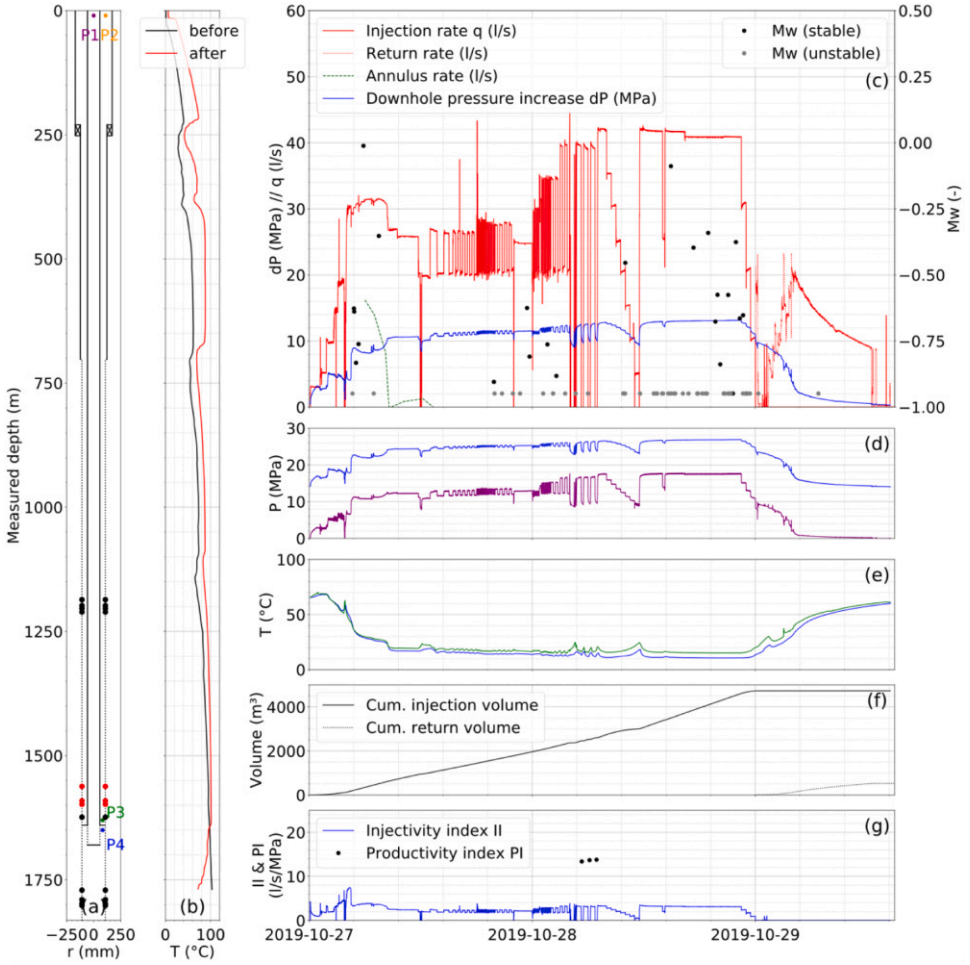

Fig. 13. Summary of injection Stage 3 with packer at 1640 m. (a) Well schematic, monitoring points and tight spots during reaming before (23 October 2019; black dots) and liner installation attempt after (30 October 2019; red dots) the stage, (b) temperature profile before (25 October 2019; black) and after (8 November 2019; red) this stage, (c) injection rate q, return rate, annulus rate and downhole pressure increase above the initial reservoir pressure measured above (P3) and below (P4) the packer, and the moment magnitude of induced seismic events, (d) all pressures measured at the monitoring points P1-P4, (e) the fluid temperatures measured downhole, (f) the cumulative injected volume, and (g) the injectivity and productivity index based on the analysis of the fall-off curves during shut-in periods.

Based on calculations with PhreeqC, the water is undersaturated of most minerals with only quartz and some iron minerals (hematite, goethite) showing positive saturation indices.

The water isotopes $d^{18}O$, $d^{17}O$, dD are natural, conservative tracers signifying a fingerprint for a certain type of water. Changes in their composition indicate mixing or dilution. Measured values here correlated well with each other (Fig. 18; $d^{17}O$ not shown). All values decreased over time (dD from −56 to −60; $d^{18}O$ from −8.2 to −9). However, in contrast to the other elements, there are two significant features in the data: (1) a positive peak at 2:45 am and (2) steep decrease between 5:30 and 6:30 am.

4.4. Stage 4: Packer at 500 m

The last stage was meant to test the integrity of the casing above 500 m and to test the complete open hole section of the well without the casing leak. Therefore, first water was injected into the annulus at 3 l/s. The pressure above the packer increased only by ~0.2 MPa while the pressure below the packer remained constant confirming the leak in the casing and a sealing packer.

Second, injection into the drill string started at the same injection rate of 3 l/s with a pressure increase below the packer by ~1.2 MPa. This shows that the casing leak is significant as compared to the flow of the open hole section of the well, which is also indicated by the difference in injectivity shown in Fig. 19g. The hydraulic performance of the open hole section itself is highly pressure dependent with an injectivity of ~2 l/s/MPa at flow rates below 10 l/s and ~11 l/s/MPa at 60 l/s. The productivity index instead is significantly higher with values between 16.6 l/s/MPa for the shortest shut-in duration and 11 l/s/MPa for the longest one. During Stage 4 no induced seismicity occurred.

5. Discussion

The hydraulic stimulation of well RV-43 in October 2019 is the first reported recent treatment of a low temperature well in Reykjavik and the first target-oriented multi-stage stimulation attempt with a straddle packer assembly in Iceland. Future stimulation treatments in the area will greatly benefit from the experiences gained by the RV-43 stimulation experiments. Due to the vicinity of the well to the city center of Reykjavik, special emphasis was given on seismic risk assessment and mitigation. Risk mitigation measures included the application of a cyclic stimulation concept, multi-stage stimulation, and the application of a conventional and an adaptive traffic light system based on high resolution real-time seismic monitoring.

5.1. Hydraulic performance of well RV-43

The initial productivity of well RV-43 was 1.4 l/s/MPa as determined by an airlift test after drilling in 2001. The three-day open hole stimulation performed directly after drilling improved the productivity of the well by a factor of 2.8 to 3.9 l/s/MPa as determined by an airlift test performed after stimulation in 2001.

The initial injectivity of well RV-43 in 2019 was 3.6 l/s/MPa at 2.5 MPa overpressure. This initial injectivity is similar to the final productivity of the well in 2001. The multi-stage stimulation in 2019 increased the injectivity of well RV-43 by a factor of ~3.5 to 12.5 l/s/MPa at 2 MPa overpressure (Stage 1). The corresponding productivity index was 12.3 l/s/MPa (Stage 2). Thus, injectivity and productivity of the well are

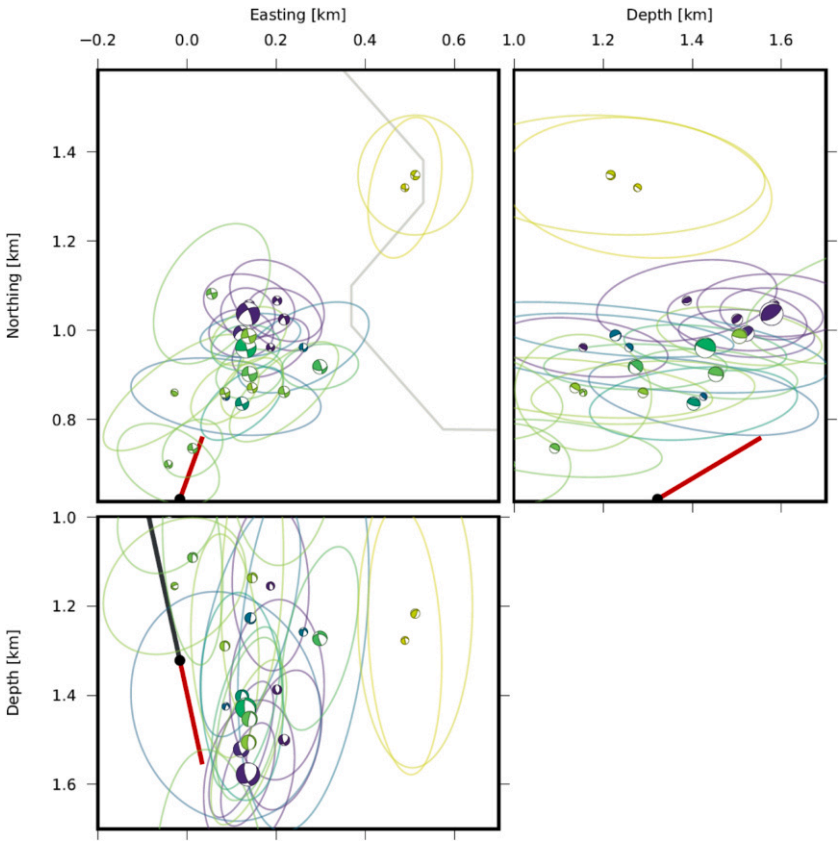

Fig. 14. Horizontal view and vertical projections of the well-path of RV-43 (above packer in black and injection interval below packer in red), locations of seismic events during Stage 3 and their error ellipsoids. Symbols in the epicentral map show lower hemispherical projections of the double-couple component of the moment tensor. Side views show side-projections, respectively. Colours indicate time of occurrence (see Figs. 14 and 15 for scale). Unstable moment tensor solutions are not shown here.

similar. However, part of the injectivity increase is attributed to a casing leak. In the beginning of Stage 4 the injectivity index of the casing leak and the open hole section were determined for low injection rates of 2–3 l/s. With an II of 5.0 l/s/MPa determined for the casing leak and 2.2 l/s/MPa for the open hole section it can be estimated that about 2/3 of the fluid injected in or produced from the well can be attributed to the casing leak and 1/3 to the open hole section if the entire well is open to flow.

Hydraulic data of the open hole section without casing leak shows a pressure dependent injectivity index between 1.4 and 10.7 l/s/MPa and a calculated productivity index of 11–16.6 l/s/MPa (Fig. 20, Stage 4). Note that the injectivity indices are lower bounds as the test durations were too short to achieve steady-state conditions during step-down (Fig. 19) and that the productivity indices are upper bounds for the same reason. The final injection fall-off analyses of the open hole section showed a productivity index of 11 l/s/MPa without casing leak. This is ~2.8 times higher than the productivity in the final airlift tests in 2001.

Well test analysis results are summarized in Table 4. Productivity and injectivity data of all stages are summarized in Table 5. All four injection stages in 2019 show very distinct hydraulic behavior (Fig. 20):

In Stage 1 water was injected into the whole wellbore due to crossflow around the top and bottom packers. This includes the casing, which was later found to leak somewhere between 230 and 400 m MD (likely at ~230–250 m MD). During the initial step rate test the downhole pressure increased by ~2.5 MPa at 9 l/s injection rate (II = 3.6 l/s/MPa). Above 2.5 MPa the linear slope between pressure and flow rate becomes less steep. This is a typical signature for fracture opening (fracture opening pressure of Stage 1 P_{o1} = 2.5 MPa). Extrapolation of this trend to zero flow rate gives the fracture closure pressure of Stage 1 P_{c1} = 2.2 MPa. At an overpressure of 2.0 MPa water was injected with 25 l/s at the end of the stage (II = 12.5 l/s/MPa). This final injectivity is ~3.5 times higher compared to the initial II of 3.6 l/s/MPa at the same pressure level. Though, a significant part of the injectivity increase should be attributed to the casing leak.

Stage 2 experienced crossflow at an overpressure of 2.8 MPa at 5 l/s (II < 1.8 l/s/MPa). This low injectivity without crossflow indicates a significantly lower hydraulic performance below the packer at 1484 m MD as compared to the section above. With crossflow the hydraulic performance follows exactly the pressure-flow rate curve at the end of Stage 1. The shut-in analysis at the end of Stage 2 results in a calculated PI of 12.3 l/s/MPa for the entire wellbore, which is a ~3.2 fold increase compared to the productivity from the airlift test after the stimulation in 2001, and which is almost identical to the II of 12.5 l/s/MPa determined at the end of Stage 1 for the same section of the well.

At Stage 3 the packer was set at 1640 m and crossflow occurred at an overpressure of 3.2 MPa at 3 l/s (II < 1 l/s/MPa). After crossflow stopped a maximum overpressure of 13.1 MPa at 41 l/s (II = 3.1 l/s/MPa) and an overpressure at the end of the stage of 11 MPa at 10.5 l/s (II = 1 l/s/MPa) were observed. While the injectivity does not seem to have changed, the difference in slope of the flow rate-pressure curves in Fig. 20 indicates fracture opening as well. Shut-in analyses during Stage 3 show consistent productivity indices between 13.4 and 13.8 l/s/MPa, which is even above the PI of 12.3 l/s/MPa calculated for the whole wellbore before. The difference of productivity (>13.4 l/s/MPa) and injectivity (~1 l/s/MPa) can be attributed to the imbalance of stimulated volume in a confined depth section (i.e. a confined fracture that is opened, but that is not connected to a permeable structure where a significant part of the injected fluid could leak-off). This is leading to a high overpressure, which is released during flow-back.

During Stage 4 first the casing leak was confirmed with an overpressure of 0.6 MPa at 3 l/s injection rate (II = 5 l/s/MPa). This is higher as compared to the initial injectivity in Stage 1, which indicates that the leak was either caused or enlarged by the stimulation or the formation behind the leak was stimulated. Stepwise flow rate increase during injection into the open hole below the casing shows an initial injectivity of 2.2 l/s/MPa (dP = 1.2 MPa at q = 2.6 l/s), which is lower than the

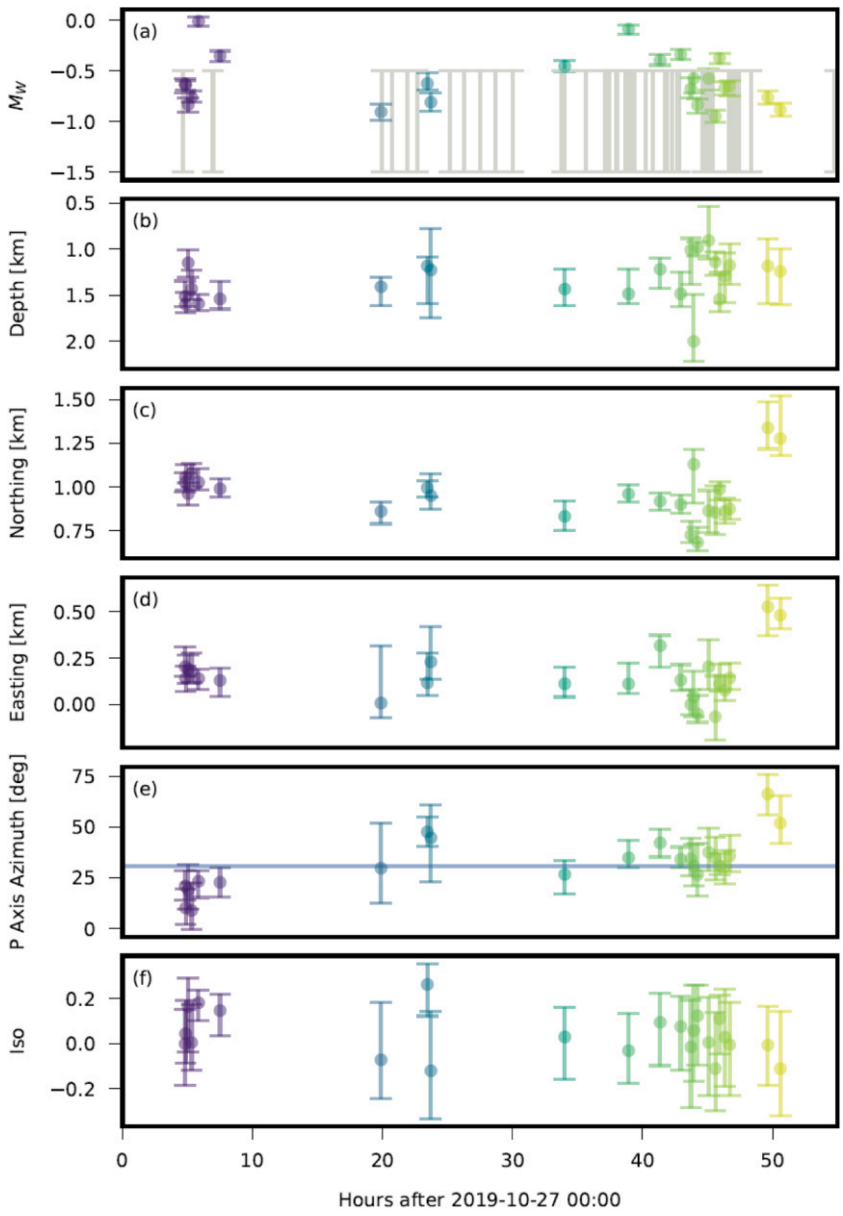

Fig. 15. Development of moment magnitude (a), location (b-d), P Axis azimuth (e) and isotropic part (f, volume change relative to seismic moment, for definition see e.g. Dahm and Krüger, 2014) of all seismic events with time.

injectivity of the casing leak. At higher pressures the gradual change in slope up to 4.6 MPa at 19.5 l/s (II = 4.2 l/s/MPa) indicates opening of a pre-existing fracture. A maximum overpressure of 5.5 MPa was reached at 59 l/s (II = 10.7 l/s/MPa), but the step rate decrease afterwards shows no significant deviation from the initial step rate increase at the start of the test. This can be interpreted as elastic fracture opening and closure. Calculated productivities during this stage range from 16.6 l/s/MPa for short tests to 11.0 l/s/MPa for the longest test. Since the well was still flowing after Stage 3 the hydraulic behavior of Stage 4 may have been significantly distorted by an additional flow from the bottom of the well that leads to higher pressure increases. Additionally, several reaming operations in between the stages may have influenced the hydraulic performance of the well (Table 1). It is interesting to note that fracture opening or crossflow started at a similar level of overpressure between 2.4 MPa and 3.2 MPa in all four stages (Fig. 20).

In summary, Stage 1 (entire well) showed a permanent permeability increase largely attributed to a casing leak. Stage 2 (entire well) confirmed the results of Stage 1. Stage 3 (below 1640 m) was interpreted as inflation of an isolated fracture with no connection to highly permeable structures. Stage 4 confirmed the casing leak and showed elastic opening and closure of an existing fracture without permanent permeability increase.

At other EGS sites similar observations were made. For example, a similar pressure dependent fracture opening and closure without permanent permeability increase was observed in the Urach 3 borehole (Stober, 2011). At Bad Urach, this was interpreted as elastic behavior of the fracture with limited shear displacement indicated by low magnitude seismic events (Mw<1.8). On the other hand, a permanent permeability increase due to hydraulic stimulation was observed for example at Soultz-sous-Forêts. At Soultz, larger induced seismic events (Mw < 2.9) occurred, indicative for larger shear displacements that may have resulted in a permanently increased fracture aperture (Stober, 2011). Another example is the Pohang EGS well PX-1, where the first stimulation resulted in a permanent permeability increase, while a second stimulation treatment performed in the same interval for a shorter duration with lower pressures, lower volumes, and lower flow

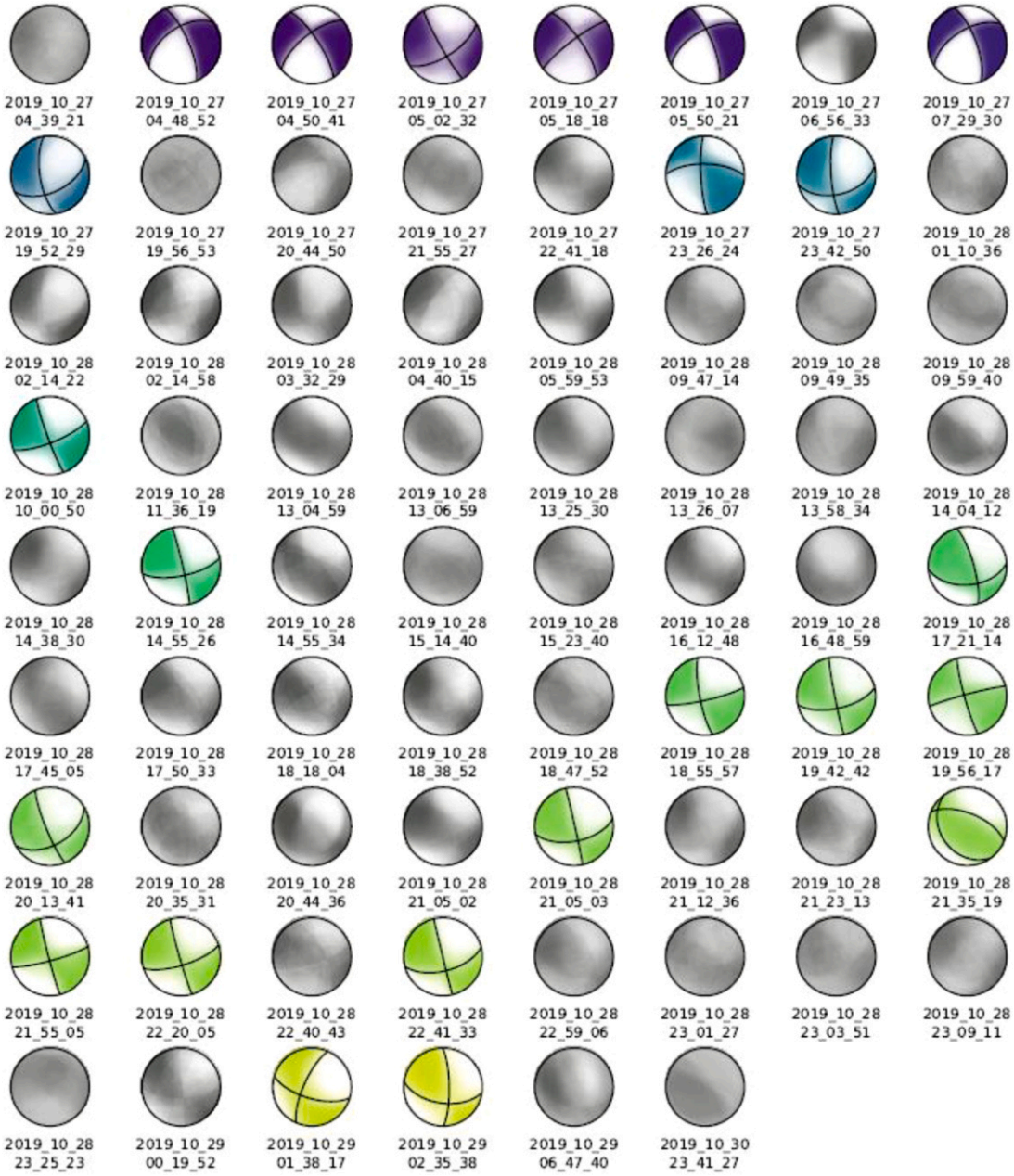

Fig. 16. Moment tensor solutions of the 70 induced seismic events. Continuous lines indicate the best double couple, smeared colors the radiation pattern of the full probabilistic (fuzzy) moment tensor. Unstable (fuzzy) solutions are shown in gray. Stable solutions are colored according to the time of occurrence.

rates did not result in an additional permeability increase (Hofmann et al., 2019; Park et al., 2020).

Overall a larger hydraulic, thermal, mechanical or chemical perturbance as compared to past injections into a well seem to be required to further improve the hydraulic performance of an already stimulated well. This may be achieved by stimulating different sections of the well, by using different injection fluids or by injecting larger fluid volumes, at higher pressures/flow rates, with lower temperatures, or for a longer time. For a permanent permeability increase, self-propping by shear displacement is required if no proppants are used. In a single-well system the stimulated near wellbore area or fracture networks need to be connected to a permeable zone for a successful stimulation. In multi-well systems injection and production wells need to be hydraulically connected by the stimulated structures.

Fig. 21 shows the pressure response to all four stages in the vertical well HS-33 located ~700 m south of RV-43. HS-33 is only 340 m deep. During Stages 1, 2 and 4 a clear pressure increase by up to 0.05 MPa was observed. During Stage 3 initially the pressure slightly increased in HS-33 during crossflow around the packer in RV-43, but no effect was observed after returns stopped from the RV-43 annulus. This observation highlights that a separate zone was stimulated during Stage 3 with no influence on well HS-33. No indication for a hydraulic connection between the open hole section below 702 m MD and the casing leak at ~250 m MD was found. For example, the pressure above the packer stayed constant during Stage 4 injection into the open hole and no return flow was observed.

A future production test would indicate whether flow rates and temperatures are sufficient to bring the well online. The produced water will be coming from different zones from 250 m down to 1550 m TVD. This will require further analysis of the geochemistry and hydrogeology to avoid unintended chemical reactions due to mixing of different fluids. Modeling studies or flow logs could indicate how the different zones

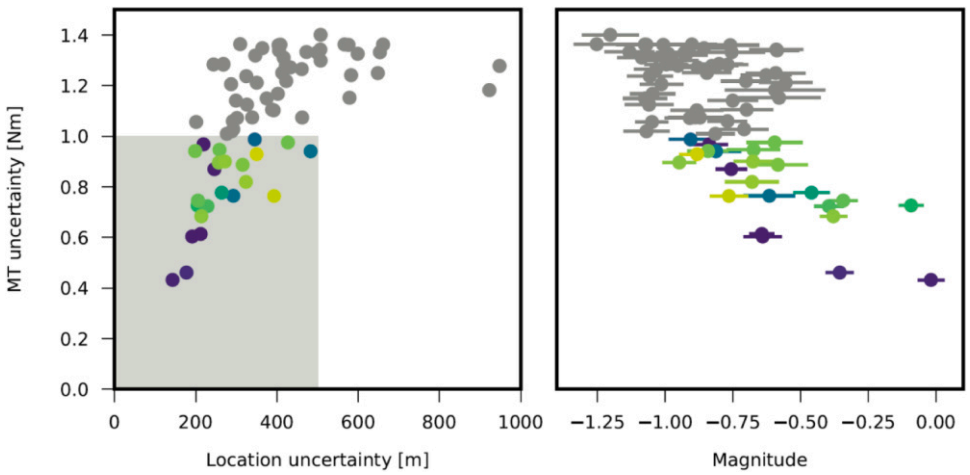

Fig. 17. Location and magnitude uncertainties for all 70 seismic events. Moment tensor solutions were categorized in stable (colored) and unstable (gray).

contribute to flow. Flowmeter logs or models of the measured thermal anomalies resulting from cold water injection could permit to estimate how much water was injected into the different zones and how much the different zones contribute to flow.

5.2. Cyclic injection

No significant differences between constant rate injection, cyclic injection and pulse injection were found when the maximum flow rates were the same. However, short phases of high rate injection were more effective than long constant rate injection phases (Fig. 22).

While high injection rates seem to be important for the hydraulic performance increase it is unclear whether short high injection rate phases significantly influence the seismic risk. The limited seismicity during the different stimulation stages does not allow a conclusive comparison between different injection schemes. However, seismic activity and magnitudes were lower during cyclic injection phases. Only three stable events with Mw < -0.75 and eight unstable events were detected during cyclic injection while 59 seismic events were registered during continuous injection phases of Stage 3 with moment magnitudes of up to -0.01 (Fig. 12). On the other hand, the longest continuous injection phase was performed after the cyclic injection, and a common observation for many stimulation experiments is that the magnitudes of induced earthquakes increase with the injected volume and duration of operation.

5.3. Induced seismicity during 2019 stimulation of RV-43

Seismic activity occurred exclusively during the injection phase of Stage 3. With only 70 seismic events during this deepest stimulation stage at 1484 m with moment magnitudes between -1.00 and -0.01 the seismic hazard and risk, a concern due to the closeness to Reykjavik, was very low, and substantially lower than assumed in the a-priori risk study (Broccordo et al., 2020). While seismicity was still observed during the flow rate reduction phase at lower levels, flowback at the end of the stage stopped all seismic activity. The demonstration of the updating of the a-prior risk assessment in near-real-time performed as expected, with the individual risk dropping by a factor of 100. However, because so few events have been recorded, the uncertainty in the risk assessment was not reduced much (Fig. 11, dashed lines).

Despite the events being so tiny, the full waveform analysis and probabilistic moment tensor approach still allowed to characterize the sources and to identify the sub-vertical stimulated target structures which strike similar to the major fault orientations in the area (N-S and NE-SW) and confirmed the stress state to be strike-slip with a maximum horizontal stress direction of ~N30°E. Based on this experience, future projects can be planned with a better knowledge on the drilling target, seismic risk, stress field and structural geology. The low number and magnitudes of induced seismic events as well as the past experiences of stimulations near Reykjavik suggest that future hydraulic stimulations of similar wells in Reykjavik may not pose a substantial seismic risk.

The relation between injected fluid volume and maximum induced seismic magnitude in Fig. 23 suggests that in this stimulation, no critically prestressed fault was reactivated and that also continued injection into Stage 3 would likely not have caused seismic events above the traffic light thresholds. It is less clear to what extend these findings can be extrapolated to other wells in the Reykjavik area. Given the heterogeneity of the seismic response to injection, the heterogeneity of the stress field and the unknown location of potentially critically stressed faults, we suggest that future projects near populated areas in Iceland should also implement a high-resolution seismic network and risk assessment and mitigation strategies as outlined here.

It is worth noting that we applied here for the first time an adaptive traffic light system that updates individual risk assessments in near-real time during a geothermal hydraulic stimulation project. Past EGS projects, such as the one in Helsinki (Kwiatek et al., 2019), only computed updated forecasts of event numbers, not hazard or risk. While we were able to demonstrate the operational and communication procedures successfully, the limited amount and low magnitudes of induced seismicity did not allow to demonstrate the full advantages of ATLS. Nevertheless, the demonstration project on Geldinganes confirmed that ATLS procedures have the potential to be a significant step forward for seismic risk mitigation, a necessary step in light of the experience at the Pohang site and suggested by Lee et al. (2019). A conventional TLS such as the one shown in Fig. 8 should, however, always be implemented as a first order mitigation procedure.

5.4. Chemical interpretation of Stage 3

The change in chemical composition of the samples indicated that the injected water diluted successively with the reservoir water over time. The composition of the reservoir water is uncertain, but some unpublished data from chemical analysis of the RV-43 well taken in 2010 are available that indicate its composition (Table 3). This allows roughly to estimate the share of reservoir fluid in the flowback. Best estimates could be obtained when considering the more conservative ions K, Na, Cl, SO_4, and SiO_2. For some ions (SO_4, K, SiO_2) a similar percentage of about 54–58% were obtained. However, this comparison also shows that a range of chemical reactions is ongoing such as corrosion of the casing which explains the relatively high Fe concentration in the back flow and which may have contributed to the casing leak.

A correlation of the chemical composition with the well operations is

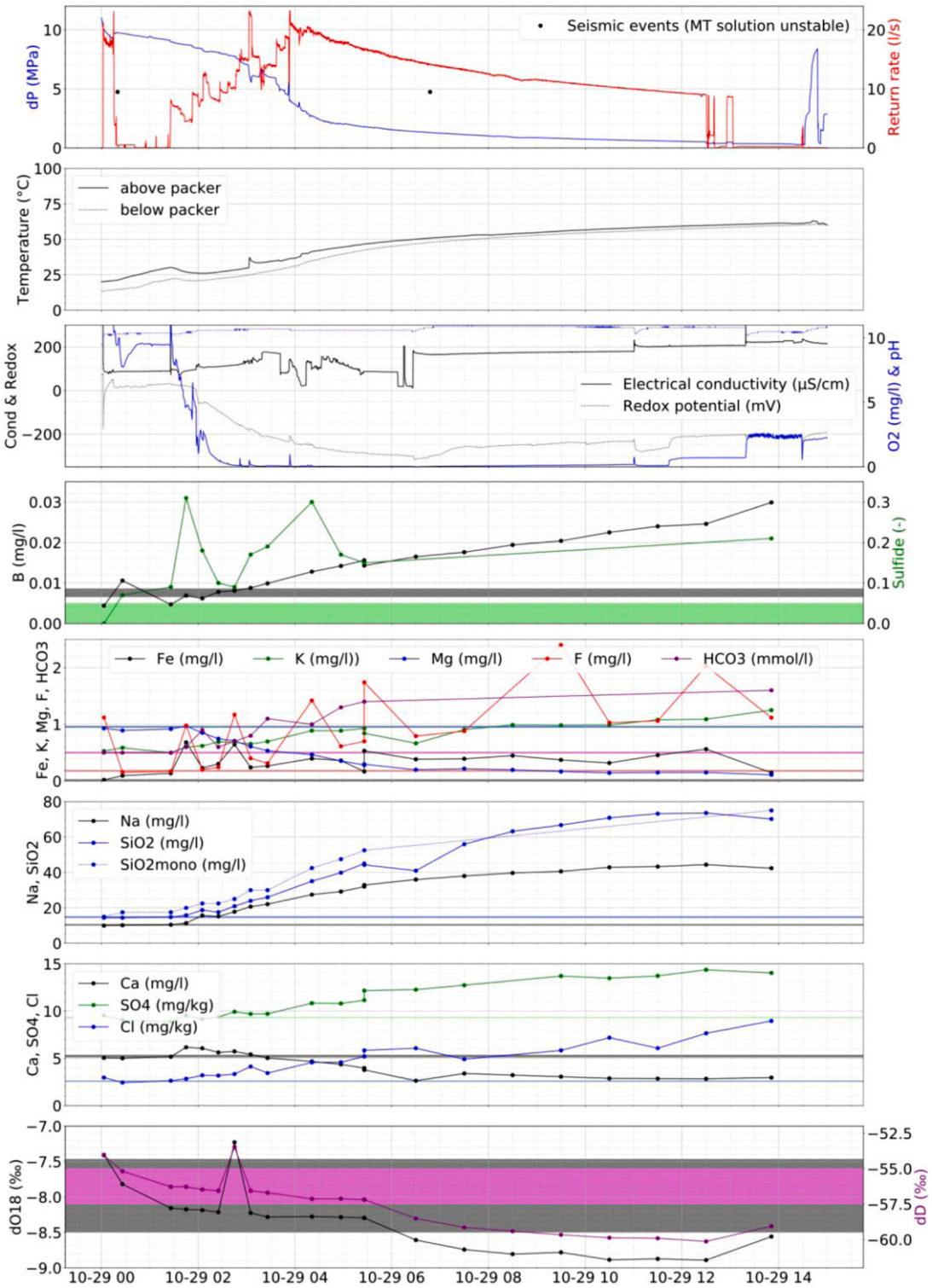

Fig. 18. Development of hydrochemistry in comparison to thermal, hydraulic and seismic data during the flowback period of Stage 3 on 29 October 2019. Shaded areas in the background show the range of values determined for the injection fluid.

not obvious. The data predominantly indicate a mixing of two types of water. Neither seismic events nor pressure changes correlate with the chemical composition in the flow back (Fig. 18). On the other hand, chemistry might reveal processes that are not obvious from the physical data. Especially the steep drop of dD and $d^{18}O$ indicates a mixing of another reservoir water (different depth/age) with very similar composition. Although this drop was not observed in the concentration curves of other chemical elements measured, it approximately coincides with the redox values measured in the flow-through cell that increased again around 7am (Fig. 18), which also indicates a change in reservoir conditions.

5.5. Zonal isolation and wellbore conditions

The hydraulic stimulation treatment would have been more efficient if the casing had not been damaged and logging and zonal isolation had

Table 3
Comparison of the chemical compositions of water flowing out of the well in 2010, the last sample of the water flowing out of the well at the end of the flowback period of Stage 3 in 2019, and a sample of the injection water. The relative percentage of reservoir fluid was estimated based on the comparison of these three samples.

	Sample 2010	Sample injected water 2019	Sample last collected 2019	% of reservoir fluid
T (°C)	68	RT	73	
El. cond. (µS/cm)	200	nm	205	
pH	9.6	nm	10.8	
CO_2-water (mg/kg)	25.5	Nm		
H_2S-water (mg/kg)	2.9	<0.05		
O_2 (mg/kg)	0.0	oxic	0.7	
Cl (mg/l)	24.2	2.6	7.7	38.3
SO_4 (mg/l)	30.1	9.3	13.4	57.5
SiO_2 (mg/l)	143.5	14.5	73.6	55.7
Na (mg/l)	67.9	10.2	44.4	69.9
K (mg/l)	2.4	0.5	1.1	54.2
Ca (mg/l)	2.5	5.1	2.8	
Mg (mg/l)	0.95	0.90	0.20	
Fe (mg/l)	0.0	0.0	0.6	
B (mg/l)	0.09	0.01	0.02	31.0

been more successful.

The limited logging data due to the poor wellbore conditions forced us to perform the stimulation stages from top to bottom. As a result, the well was not accessible after injection below Stages 1 and 3. Therefore, costly and time-consuming reaming operations had to be performed after these stages (Table 1). Future multi-stage stimulation should be done from bottom to top in open hole wells to avoid this.

During all four stages the packers were set successfully. Also, the almost 150 m long inflation line between bottom and top packer of Stage 1 was not damaged during the operation by clamping it on the high side of the drill string. Continuous zonal isolation throughout the whole stage was only achieved in Stage 4, where a single packer was placed inside the casing. Stage 1 showed crossflow from the beginning, possibly due to the vicinity to fracture areas. Stage 2 experienced crossflow after a short initial pressure increase. This is interpreted as opening of a flow path at this maximum pressure and subsequent flow around the packer. Stage 3 behaved similar to Stage 2 in the beginning, but after continued injection with open annulus crossflow stopped over time completely and zonal isolation was achieved for most part of this stage. There can be different explanations for this behavior. First, all injected water may have been taken by the permeable zones above the packer. This is unlikely since the crossflow was reduced with increasing flow rate. Second, the crossflow path may have been clogged by fines due to continuous high injection rate. Lots of fine material above and in between the packers supports this speculation, but we did not see sediments in the tanks at the surface. Third, the crossflow path may have been clogged by mineral precipitation due to the change in pressure and temperature and the different chemical composition (e.g., elevated Ca) of the injection water compared to the reservoir water. Fourth, shearing of existing fractures may have shifted the flow path. This appears unlikely, as the seismicity occurred after the pressure increase, but may be a consequence of aseismic creep. The unexpected sealing of the packer during

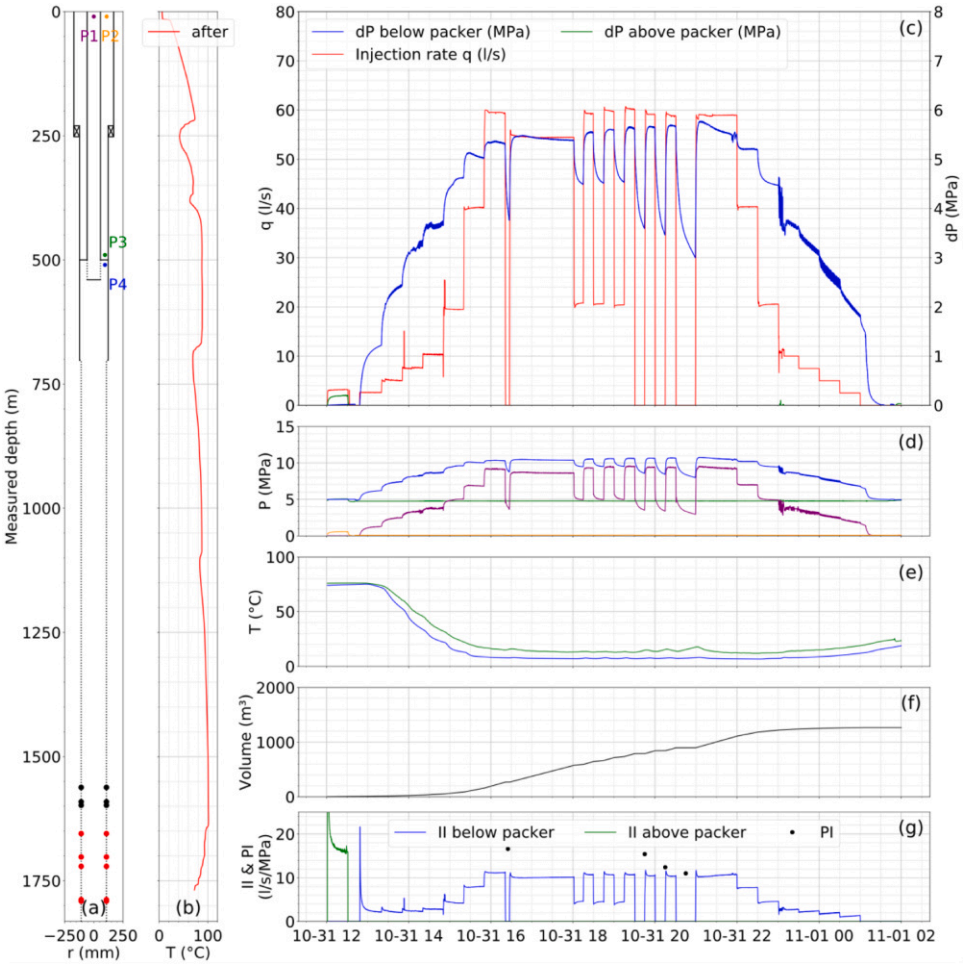

Fig. 19. Summary of injection Stage 4 including an initial casing integrity test with packer at 500 m. (a) Well schematic, monitoring points and tight spots identified during the liner installation attempt on 30 October 2019 (before the stage; black dots) and during reaming on 1 November 2019 (after the stage; red dots), (b) temperature profile after (8 November 2019) this stage, (c) injection rate q and downhole pressure increase above the initial reservoir pressure measured above (P3) and below (P4) the packer, (d) all pressures measured at the monitoring points P1-P4, (e) the fluid temperatures measured downhole, (f) the cumulative injected volume, and (g) the injectivity and productivity index based on the analysis of the fall-off curves during shut-in periods.

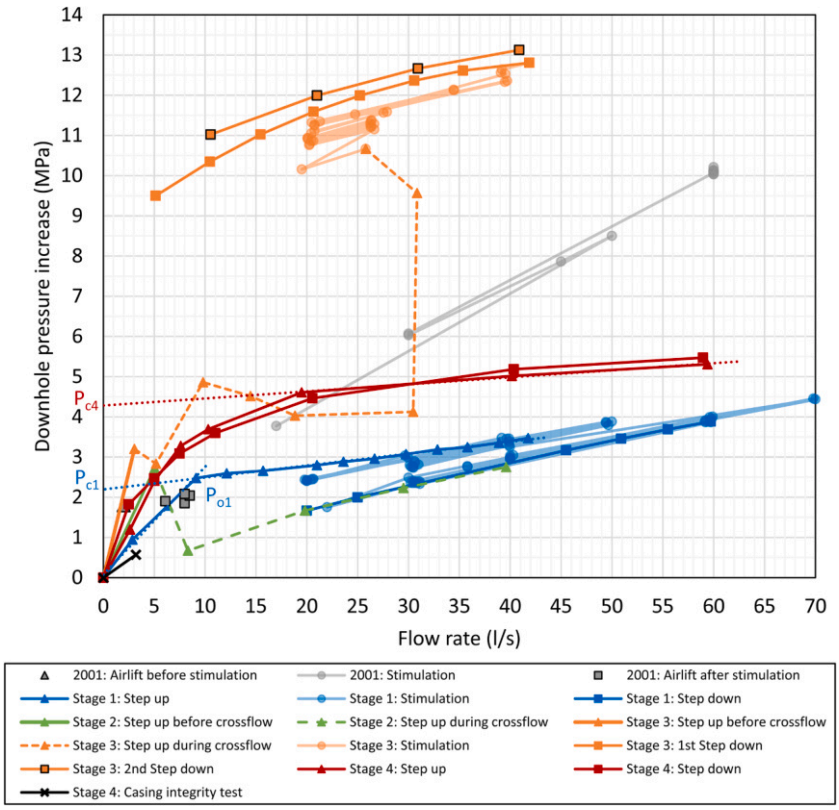

Fig. 20. Injection rate and downhole pressure increase for all four injection stages in 2019 and the initial well stimulation in 2001. For the airlift tests production rate and pressure decrease are plotted. Linear trends are shown by dotted lines, fracture opening pressures Po are highlighted at the intersection of each of the two trends and fracture closure pressures Pc are highlighted at the intersection with the pressure axis.

Table 4
Summary of well test analysis results from shut-in periods in all stages.

Stage	Transmissivity kh (m^3)	Skin s (-)	Compressibility c (m^3/MPa)	Productivity Index PI (l/s/MPa)
1–1	4.43e-13	−3.62	1.86	0.7
1–2	7.82e-13	−3.45	2.67	1.1
1–3	1.05e-12	−3.57	1.46	1.5
1–4	1.59e-12	−3.59	2.20	2.3
1–5	2.42e-12	−3.26	4.24	3.3
1–6	2.16e-12	−3.61	2.54	3.2
1–7	3.61e-12	−3.21	5.23	4.9
1–8	4.30e-12	−3.11	4.62	5.7
1–9	5.46e-12	−2.82	6.79	6.8
1–10	6.41e-12	−2.51	6.71	7.5
1–11	5.99e-12	−2.86	6.30	7.5
2–1	4.15e-12	−5.76	0.54	12.3
3–1	5.78e-12	−5.17	1.18	13.4
3–2	5.44e-12	−5.38	1.04	13.7
3–3	5.57e-12	−5.34	1.26	13.8
4–1	9.41e-12	−4.31	3.24	16.6
4–2	9.18e-12	−4.31	3.75	15.4
4–3	7.31e-12	−4.18	4.20	12.4
4–4	6.24e-12	−4.31	4.31	11.0

Stage 3 injection after early crossflow should be further analyzed in the future.

Temperature logs and an injection test in the annulus during Stage 4 (packer at 500 m) revealed a casing leak. This was found at the depth level of the uncemented connection interval between the casing from 0 to 252 m MD and the liner from 230 to 702 m MD (Fig. 10). This significantly complicates the analysis of the stimulation results and highlights that future injection operations require a casing integrity test, especially in old wells and wells with uncemented casing and liner hanger.

5.6. Implications for site development on Geldinganes

The target of well RV-43 was a strong temperature gradient anomaly that strikes ~NE-SW, which is probably caused by a fault zone. The dip of the corresponding fault was believed to be +−3°. The well was designed to intersect this potentially permeable structure. Induced seismic events now suggest that this drilling target may have been stimulated. The sub-vertical structure stimulated during the 2019 stimulation strikes NNW-SSE (according to focal mechanism solutions) to NE-SW (best fitting plane through all seismic events). New wells on Geldinganes may target this stimulated structure with the chance of intersecting additional subparallel flow zones. This would require a well azimuth towards NW, perpendicular to the maximum horizontal stress direction of ~N30°E and primary faults striking ~N42°E and ~N5°E. This would increase the chance of intersecting open fractures, allow to open fractures perpendicular to the well by stimulation treatments, and reduce the possibility of crossflow around packers through fractures parallel to the well. Well RV-43 may be used as monitoring well and future producer in addition to new wells.

Hydraulic stimulation treatments of similar wells with straddle packers should be performed right after drilling to save costs for mobilization and de-mobilization of rig, pumps and crew. This will also reduce the risks associated to older wells such as wellbore stability and integrity.

Overall, we found that hydraulic stimulation is a promising technology to significantly improve the hydraulic performance of low temperature geothermal wells in Reykjavik. Soft stimulation measures, such as cyclic injection, multi-stage stimulation and adaptive traffic light systems provide a promising framework to do so while managing the site-specific seismic risk.

Table 5
Injectivity (II) and productivity (PI) indices at the beginning (initial), at the end (end), at maximum flow rate (at qmax) and during (during) each stimulation stage. The folds of increase (FOI) describes the productivity and injectivity enhancement compared to the final PI in 2001 (3.9 l/s/MPa) and the initial II in 2019 (3.6 l/s/MPa), respectively.

Stimulation stage	Depth range (m)	II initial (l/s/MPa)	II at q_{max} (l/s/MPa)	II end (l/s/MPa)	PI initial (l/s/MPa)	PI during (l/s/MPa)	PI end (l/s/MPa)	FOI (-)
2001	230 – 1832	–	6.0	–	1.4	–	3.9 (3.9–4.2)	2.8 (PI)
Stage 1 2019 crossflow	0 – 1832	3.6 (3.0–12.0)	15.8	12.5	0.7 – 7.5	–	–	3.5 (II)
Stage 2 2019 crossflow	0 – 1832	11.0	14.0	14.0	–	–	12.3	3.2 (PI) 3.9 (II)
Stage 2 2019	1484 – 1832	<1.8	–	–	–		–	–
Stage 3 2019	1640 – 1832	<1.0	3.1	1.0	–	13.4 – 13.8	–	3.4–3.5 (PI)
Stage 4 2019	500 – 1832	2.2	10.7	1.4	–	11.0 – 16.6	–	2.8–4.2 (PI)
Stage 4 2019 annulus (casing leak)	0 – 500	5.0	–	–	–	–	–	–

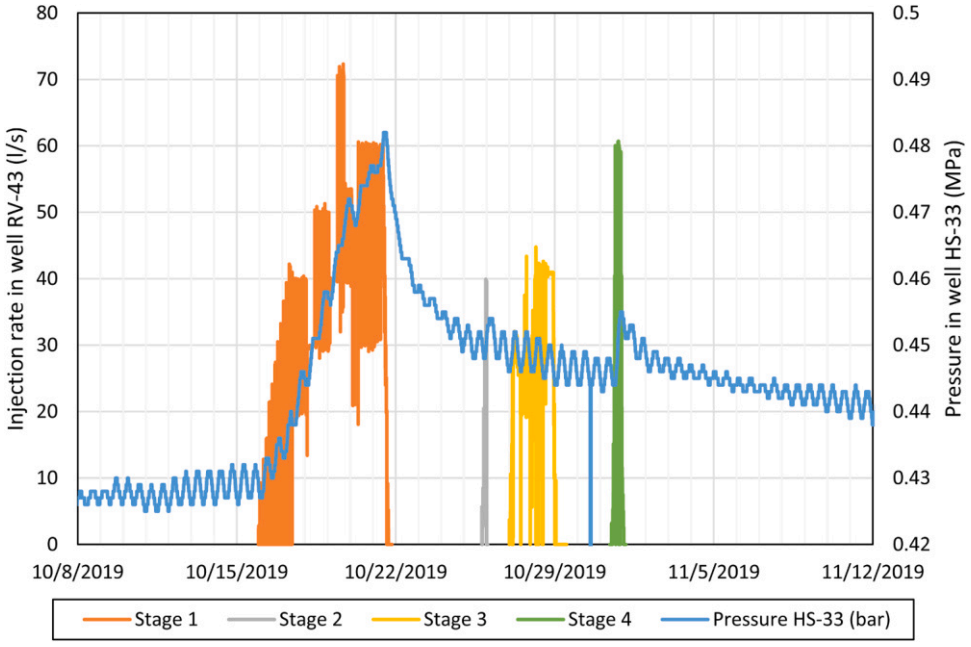

Fig. 21. Pressure increase in vertical well HS-33 due to injection in RV-43. HS-33 is located ~700 m south of RV-43. The well is only 340 m deep. Except for Stage 3 (injection below 1640 m) all injection activities in RV-43 resulted in a pressure increase in HS-33.

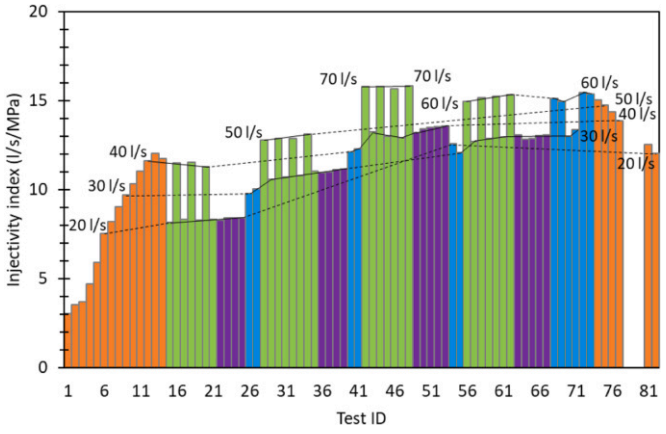

Fig. 22. Injectivity index at the end of each constant injection rate phase during Stage 1 (orange=step rate injection, green=cyclic injection, purple=pulse injection, blue=constant injection). For constant injection the first data point is after 1 hour of injection. Injection rates are annotated.

6. Conclusions

The hydraulic stimulation of well RV-43 in October 2019 is the first reported recent treatment of a low temperature well in Reykjavik and the first target-oriented multi-stage stimulation attempt with a straddle packer assembly in Iceland. Future stimulation treatments in the area will greatly benefit from the experiences gained by the RV-43 stimulation experiments.

Due to the vicinity of the well to the city center of Reykjavik, special emphasis was given on seismic risk assessment and mitigation. Risk mitigation measures included the application of a cyclic stimulation concept, multi-stage stimulation, and the application of a conventional and an adaptive traffic light system based on high resolution real-time seismic monitoring.

The injectivity of the well was increased by a factor of ~3.5 to 12.5 l/s/MPa at 2 MPa differential pressure. However, a significant part of this injectivity increase is attributed to a casing leak. The final injection fall-off analyses of the open hole section without casing leak showed a productivity index of 11 l/s/MPa, which is ~2.8 times higher than the productivity in the final airlift tests in 2001. However, the injectivity of the open hole was highly pressure dependent and indicative for elastic

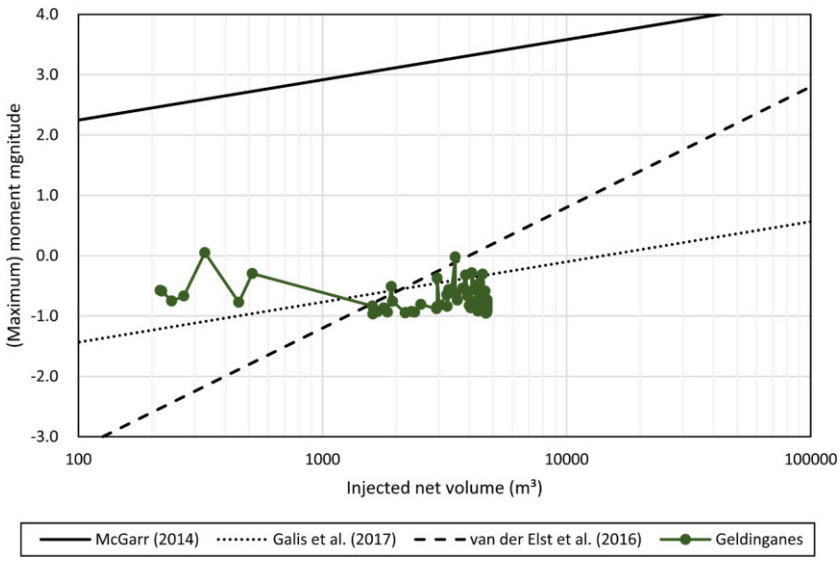

Fig. 23. Relationship between injected net volume and maximum moment magnitude. Observed moment magnitudes from moment tensor analysis of induced seismic events during Stage 3 are plotted. Continuous and dashed lines show the theoretical relationships of injected volume and maximum moment magnitude by McGarr (2014), Galis et al. (2017) and van der Elst et al. (2016) with the following parameters: G = 30 GPa (McGarr 2014), γ = 2000 (Galis et al., 2017), b = 0.5 and Σ=−3.6 (van der Elst et al. 2016).

fracture opening and closure. The hydraulic stimulation treatment would have been more efficient if the casing had not been damaged and logging and zonal isolation had been more successful.

With only 70 seismic events during the deepest stimulation stage at 1484 m with moment magnitudes between −1.00 and −0.01 the seismic hazard was very low, and well below expected maximum magnitudes. Despite the events being so tiny, the full waveform analysis and probabilistic moment tensor approach still allowed to characterize the sources and to identify the sub-vertical stimulated target structures and confirmed the stress state to be strike-slip with a maximum horizontal stress direction of ~N30°E. Based on this experience, future projects can be planned with a better knowledge on the drilling target, seismic risk, stress field and structural geology.

The results indicate that short cycles of high rate/pressure injection are significantly more efficient than long constant rate injection phases with similar injection rate and pressure. No significant differences in hydraulic performance were found between constant rate injection and cyclic injection when the maximum flow rates and pressures were the same. However, seismic activity and magnitudes were lower during cyclic injection phases as compared to continuous injection phases.

The experience with RV-43, with only two out of four stages with (partially) sealing packer and no crossflow, highlights the challenges associated to zonal isolation of long, deviated and fractured open hole sections in old wells. Besides a thorough understanding of the stress field and structural geology of a region, good quality BHTV data preceded by temperature and caliper logs are the minimum requirement for successfully isolating promising stimulation target zones by inflatable open hole packers. However, it is better to design wells specifically for stimulation with an azimuth perpendicular to the maximum horizontal stress direction and the most promising fracture sets and with cased sections that allow reliable zonal isolation.

Overall, hydraulic stimulation is a promising technology to significantly improve the hydraulic performance of low temperature geothermal wells in Reykjavik. Soft stimulation measures, such as cyclic injection, multi-stage stimulation and adaptive traffic light systems provide a promising framework to do so while managing the site-specific seismic risk.

CRediT authorship contribution statement

Hannes Hofmann: Conceptualization, Methodology, Validation, Formal analysis, Investigation, Resources, Data curtion, Writing – original draft, Writing – review & editing, Visualization, Supervision, Project administration. **Günter Zimmermann:** Conceptualization, Methodology, Validation, Formal analysis, Investigation, Resources, Data curtion, Writing – original draft, Writing – review & editing, Visualization, Supervision, Project administration. **Ernst Huenges:** Conceptualization, Methodology, Writing – review & editing, Project administration, Funding acquisition. **Simona Regenspurg:** Conceptualization, Methodology, Validation, Formal analysis, Resources, Data curtion, Writing – original draft, Writing – review & editing, Supervision, Project administration. **Santiago Aldaz:** Methodology, Investigation, Writing – original draft, Writing – review & editing, Supervision. **Claus Milkereit:** Methodology, Investigation, Resources, Writing – original draft, Writing – review & editing. **Sebastian Heimann:** Methodology, Software, Validation, Formal analysis, Investigation, Data curtion, Writing – original draft, Writing – review & editing, Visualization. **Torsten Dahm:** Conceptualization, Methodology, Writing – original draft, Writing – review & editing, Supervision. **Arno Zang:** Conceptualization, Writing – original draft, Writing – review & editing. **Francesco Grigoli:** Methodology, Software, Validation, Formal analysis, Investigation, Data curtion, Writing – original draft, Writing – review & editing, Visualization. **Dimitrios Karvounis:** Methodology, Software, Validation, Formal analysis, Investigation, Writing – original draft, Writing – review & editing. **Marco Broccardo:** Methodology, Software, Validation, Formal analysis, Investigation, Writing – original draft, Writing – review & editing, Visualization. **Stefan Wiemer:** Conceptualization, Methodology, Writing – original draft, Writing – review & editing, Supervision. **Vala Hjörleifsdóttir:** Conceptualization, Methodology, Validation, Investigation, Resources, Writing – original draft, Supervision, Project administration. **Bjarni Reyr Kristjánsson:** Conceptualization, Methodology, Validation, Investigation, Resources, Writing – original draft, Supervision, Project administration. **Gylfi Páll Hersir:** Methodology, Resources, Writing – original draft, Supervision, Project administration. **Ragnheiður St. Ásgeirsdóttir:** Methodology, Investigation, Resources, Data curtion, Supervision, Project administration. **Rögnvaldur Magnússon:** Methodology, Software, Formal analysis, Data curtion. **Sigurveig Árnadóttir:** Formal analysis, Data curtion, Writing – original draft, Visualization.

Declaration of Competing Interest

The authors declare that they have no known competing financial interests or personal relationships that could have appeared to influence the work reported in this paper.

Acknowledgements

The authors are grateful for the funding received from the European Commission Horizon 2020 research and innovation program under grant agreement No. 691728 (DESTRESS). HH was additionally supported by the Helmholtz Association's Initiative and Networking Fund (contract number VH—NG-1516). FG was also financed by the European Union's Horizon 2020 Framework Programme under the Marie Skłodowska Curie Grant agreement (790900). MB was also supported by the Italian Ministry of Education, University and Research (MIUR) in the frame of the "Departments of Excellence" (grant L 232/2016). TD and SH acknowledge the support of BMBF within SECURE (03G0872). We thank the participating staff from all partner institutions involved including Sveinbjörn Hólmgeirsson, Stefan Mikulla, Nima Nooshiri, Jochem Kück, Marco Groh, Martin Töpfer, Oliver Rach, Sandra Snæbjörnsdóttir, Edda Aradóttir, Luca Scarabello, Kristján Ágústsson, Stefán Auðunn Stefánsson, Ólafur Flóvenz, Ivan Kosorok, Francis Ford and many more.

All data from the stimulation in 2019 is provided in the supplementary material. Additional data on the site may be requested by contacting the corresponding author.

Supplementary materials

Supplementary material associated with this article can be found, in the online version, at doi:10.1016/j.geothermics.2021.102146.

References

Baisch, S., Koch, C., Muntendam-Bos, A., 2019. Traffic Light Systems: to what extent can induced seismicity be controlled? Seismol. Res. Lett. 90, 1145–1154. https://doi.org/10.1785/0220180337.

Bessason, B., Ólafsson, E., Gunnarsson, G., Flovenz, O., Jakobsdóttir, S., Björnsson, S., Árnadóttir, T., 2012. Verklag vegna örvaðrar skjálftavirkni í jarðhitakerfum. Orkuveita Reykjavíkur, Reykjavik, Iceland. Technical Report (In Icelandic).

Bjarnason, I.T., Menke, W., Flóvenz, O.G., Caress, D., 1993. Tomographic Image of the Mid-Atlantic Plate Boundary in Southwestern Iceland. J. Geophys. Res. 98 (B4), 6607–6622. https://doi.org/10.1029/92JB02412.

Bommer, J.J., Crowley, H., Pinho, R., 2015. A risk-mitigation approach to the management of induced seismicity. J. Seismol. 19, 623–646. https://doi.org/10.1007/s10950-015-9478-z.

Bommer, J.J., Oates, S., Cepeda, J.M., et al., 2006. Control of hazard due to seismicity induced by a hot fractured rock geothermal project. Eng. Geol. 83, 287–306. https://doi.org/10.1016/j.enggeo.2005.11.002.

Broccardo, M., Danciu, L., Stojadinovic, B., Wiemer, S., 2017a. Individual and societal risk metrics as parts of a risk governance framework for induced seismicity. In: Paper presented at 16th World Conference on Earthquake Engineering (WCEE16). Santiago, Chile, pp. 9–13. January 2017.

Broccardo, M., Mignan, A., Wiemer, S., Stojadinovic, B., Giardini, D., 2017b. Hierarchical Bayesian Modeling of Fluid-Induced Seismicity. Geophys. Res. Lett. 44 (22), 11357–11367. https://doi.org/10.1002/2017GL075251.

Broccardo, M., Mignan, A., Grigoli, F., Karvounis, D., Rinaldi, A.P., Danciu, L., et al., 2020. Induced seismicity risk analysis of the hydraulic stimulation of a geothermal well on Geldinganes, Iceland. Natl. Hazards Earth Syst. Sci. 20 (6), 1573–1593. https://doi.org/10.5194/nhess-20-1573-2020.

Buijze, L., Van Bijsterveldt, L., Cremer, H., Paap, B., Veldkamp, H., Wassing, B., Jaarsma, B., 2019. Review of induced seismicity in geothermal systems worldwide and implications for geothermal systems in the Netherlands. Netherlands J. Geosci. 98, E13. https://doi.org/10.1017/njg.2019.6.

Dahm, T., Krüger, F., 2014. Moment tensor inversion and moment tensor interpretation. In: Bormann, P. (Ed.), New Manual of Seismological Observatory Practice. GFZ German Research Centre for Geosciences, Potsdam, pp. 1–37. https://doi.org/10.2312/GFZ.NMSOP-2_IS_3.9. NMSOP-2.

Flóvenz, Ó.G., Ágústsson, K., Gudnason, Á., Kristjánsdóttir, S., 2015. In: Reinjection and induced seismicity in geothermal fields in Iceland. Paper presented at World Geothermal Congress. Melbourne, Australia, 19-25 April.

Flóvenz, Ó.G., 1979. Jarðsveiflumælingar á höfuðborgarsvæðinu. Dýpi á lag 3. Orkustofnun/Jarðhitadeild. Reykjavík, Iceland. Technical Report (In Icelandic), OS79039/JHD17.

Galis, M., Ampuero, J.P., Mai, P.M., Cappa, F., 2017. Induced seismicity provides insight into why earthquake ruptures stop. Sci. Adv. 3 (12) https://doi.org/10.1126/sciadv.aap7528 eaap7528.

Giardini, D., 2009. Geothermal quake risks must be faced. Nature 462 (7275), 848–849. https://doi.org/10.1038/462848a.

Gischig, V.S., Wiemer, S., 2013. A stochastic model for induced seismicity based on non-linear pressure diffusion and irreversible permeability enhancement. Geophys. J. Int. 194 (2), 1229–1249. https://doi.org/10.1093/gji/ggt164.

Grigoli, F., Cesca, S., Rinaldi, A.P., Manconi, A., López-Comino, J.A., Clinton, J.F., et al., 2018a. The November Mw 5.5 Pohang earthquake: a possible case of induced seismicity in South Korea. Science 360 (6392), 1003–1006. https://doi.org/10.1126/science.aat2010.

Grigoli, F., Scarabello, L., Boese, M., Weber, B., Wiemer, S., Clinton, J.F., 2018b. Pick-and waveform-based techniques for real-time detection of induced seismicity. Geophys. J. Int. 213 (2), 868–884. https://doi.org/10.1093/gji/ggy019.

Grigoli, F., Cesca, S., Priolo, E., Rinaldi, A.P., Clinton, J.F., Stabile, T.A., et al., 2017. Current challenges in monitoring, discrimination, and management of induced seismicity related to underground industrial activities: a European perspective. Rev. Geophys. 55 (2), 310–340. https://doi.org/10.1002/2016RG000542.

Gudmundsson, A., Bergerat, F., Angelier, J., Villemin, T., 1992. Extensional Tectonics of Southwest Iceland, 163. Bulletin de la Société Géologique de France, pp. 561–570.

Gunnarsson, K., 2001. Segulmælingar og fyrirhuguð borun í Geldinganesi 2001. Orkustofnun, Reykjavík, Iceland. Technical report (In Icelandic).

Gunnlaugsson, E., Frimannson, H., Sverrisson, G.A., 2000. In: *District heating in Reykjavik –70 years experience*. Presented at World Geothermal Congress, 28 May –10 June. Kyushu - Tohoku, Japan.

Haimson, B.C., Rummel, F., 1982. Hydrofracturing stress measurements in the Iceland Research Drilling Project drill hole at Reydarfjordur, Iceland. J. Geophys. Res. 87 (B8), 6631–6649. https://doi.org/10.1029/JB087iB08p06631.

Haimson, B.C., Voight, B., 1976. In: *Stress measurements in Iceland*. Paper presented at AGU Fall Annual Meeting. San Francisco, CA, USA, 6 December 1976.

Haimson, B.C., Voight, B., 1977. Crustal stress in Iceland. Pure Appl. Geophys. 115, 153–190. https://doi.org/10.1007/BF01637102.

Häring, M.O., Schanz, U., Ladner, F., Dyer, B.C, 2008. Characterisation of the Basel 1 enhanced geothermal system. In: Geothermics, 37, pp. 469–495. https://doi.org/10.1016/j.geothermics.2008.06.002.

Heidbach, O., Rajabi, M., Reiter, K., Ziegler, M., Team, W.S.M., 2016. *World Stress Map Database Release 2016*. V. 1.1. GFZ Data Services. http://doi.org/10.5880/WSM.2016.001.

Heimann, S., Isken, M., Kühn, D., Sudhaus, H., Steinberg, A., Daout, S., et al., 2018. *Grond - A probabilistic Earthquake Source Inversion framework*. V. 1.0. GFZ Data Services. http://doi.org/10.5880/GFZ.2.1.2018.003.

Heimann, S., Kriegerowski, M., Isken, M., Cesca, S., Daout, S., Grigoli, F., et al., 2017. *Pyrocko - An open-Source Seismology Toolbox and library*. V. 0.3. GFZ Data Services. http://doi.org/10.5880/GFZ.2.1.2017.001.

Hofmann, H., Zimmermann, G., Farkas, M., Huenges, E., Zang, A., Leonhardt, M., et al., 2019. First field application of cyclic soft stimulation at the Pohang Enhanced Geothermal System site in Korea. Geophys. J. Int. 217 (2), 926–949. https://doi.org/10.1093/gji/ggz058.

Hofmann, H., Zimmermann, G., Zang, A., Min, K.-.B., 2018a. Cyclic soft stimulation (CSS): a new fluid injection protocol and traffic light system to mitigate seismic risks of hydraulic stimulation treatments. Geotherm. Energy 6, 33. https://doi.org/10.1186/s40517-018-0114-3.

Hofmann, H., Zimmermann, G., Zang, A., Yoon, J.S., Stephansson, O., Kim, K.Y., et al., 2018b. Comparison of cyclic and constant fluid injection in granitic rock at different scales. Presented at 52nd US Rock Mechanics /Geomechanics Symposium 17–20. June, Seattle, WA, USA, ARMA-2018-691.

Horne, R.N., 1995. Modern well test analysis: a computer-aided approach, 2nd edition. Petroway Inc, Palo Alto.

Huenges, E., Ellis, J., Hofmann, H., Zimmermann, G., Brehme, M., Farkas, M., et al., 2018. Concepts of soft stimulation treatments in geothermal reservoirs. GRC Trans. 42, 2435–2448.

Jefferis, R.G., Voight, B., 1981. Fracture analysis near the mid-ocean plate boundary, Reykjavik-Hvalfjördur area, Iceland. Tectonophysics 76 (3–4), 171–236.. https://doi.org/10.1016/0040-1951(81)90098-6.

Karvounis, D.C., Gischig, V.S., Wiemer, S., 2014. Towards a Real-Time Forecast of Induced Seismicity for Enhanced Geothermal Systems. In: Presented at Shale Energy Engineering Conference, 21-23 July. Pittsburgh, USA. https://doi.org/10.1061/9780784413654.026.

Karvounis, D.C., Jenny, P., 2016. Adaptive Hierarchical Fracture Model for Enhanced Geothermal Systems. Multiscale Model. Simul. 14 (1), 207–231. https://doi.org/10.1137/140983987.

Keiding, M., Lund, B., Ánadóttir, T., 2009. Earthquakes, stress, and strain along an obliquely divergent plate boundary: reykjanes Peninsula, southwest Iceland. J. Geophys. Res. 114 (B9), B09306. https://doi.org/10.1029/2008JB006253.

Király-Proag, E., Gischig, V., Zechar, J.D., Wiemer, S., 2018. Multicomponent ensemble models to forecast induced seismicity. Geophys. J. Int. 212 (1), 476–490. https://doi.org/10.1093/gji/ggx393.

Király-Proag, E., Zechar, J.D., Gischig, V., Wiemer, S., Karvounis, D., Doetsch, J., 2016. Validating induced seismicity forecast models-Induced Seismicity Test Bench. J. Geophys. Res. 121 (8), 6009–6029. https://doi.org/10.1002/2016JB013236.

Kühn, D., Heimann, S., Isken, M.P., Ruigrok, E., Dost, B., 2020. Probabilistic Moment Tensor Inversion for Hydrocarbon-Induced Seismicity in the Groningen Gas Field, The Netherlands, Part 1: testing. Bull. Seismol. Soc. Am. 110 (5), 2095–2111. https://doi.org/10.1785/0120200099.

Kwiatek, G., Saarno, T., Ader, T., Bluemle, F., Bohnhoff, M., Chendorian, M., et al., 2019. Controlling fluid-induced seismicity during a 6.1-km-deep geothermal stimulation in Finland. Sci. Adv. 5 (5), eaav7224. https://doi.org/10.1126/sciadv.aav7224.

Lee, J., 1982. Well Testing. In: SPE Textbook Series, 1. Society of Petroleum Engineers, p. 159.

Lee, K.-.K., Ellsworth, W.L., Giardini, D., Townend, J., Ge, S., Shimamoto, T., et al., 2019. Managing injection-induced seismic risks. Science 364 (6442), 730–732. https://doi.org/10.1126/science.aax1878.

Lomax, A., Virieux, J., Volant, P., & Berge-Thierry, C. (2000). Probabilistic earthquake location in 3D and layered models. In: C. H. Thurber, N. Rabinowitz (Eds.), *Advances in Seismic Event location, Modern Approaches in Geophysics* (Vol. 18, pp. 101–134). Dodrecht: Springer. https://doi.org/10.1007/978-94-015-9536-0_5.

Majer, E., Nelson, J., Robertson-Tait, A., Savy, J., Wong, I., 2012. Protocol For Addressing Induced Seismicity Associated With Enhanced Geothermal Systems. U.S. Department of Energy. Report No.: DOE/EE-0662.

Maxwell, S.C., Zhang, F., Damjanac, B., 2015. Geomechanical modeling of induced seismicity resulting from hydraulic fracturing. Lead Edge 34 (6), 678–683. https://doi.org/10.1190/tle34060678.1.

Meier, P.M., Rodríguez, A.A., Bethmann, F., 2015. *Lessons Learned from Basel: new EGS Projects in Switzerland Using Multistage Stimulation and a Probabilistic Traffic Light System for the Redcution of Seismic Risk*. In: Presented at World Geothermal Congress, 19-25. April, Melbourne, Australia.

McGarr, A., 2014. Maximum magnitude earthquakes induced by fluid injection. J. Geophys. Res. 119 (2), 1008–1019. https://doi.org/10.1002/2013JB010597.

Mignan, A., Broccardo, M., Wiemer, S., Giardini, D., 2017. Induced seismicity closed-form traffic light system for actuarial decision-making during deep fluid injections. Sci. Rep. 7, 13607. https://doi.org/10.1038/s41598-017-13585-9.

Mignan, A., Broccardo, M., Wiemer, S., Giardini, D., 2019a. Autonomous decision-making against induced seismicity in deep fluid injections. In: Ferrari, A., Laloui, L. (Eds.), *Energy Geotechnics, SEG 2018, Springer Series in Geomechanics and Geoengineering*. Springer, Cham, pp. 369–376. https://doi.org/10.1007/978-3-319-99670-7_46.

Mignan, A., Landtwing, D., Kaestli, P., Mena, B., Wiemer, S., 2015. Induced seismicity risk analysis of the 2006 Basel, Switzerland, Enhanced Geothermal System project: influence of uncertainties on risk mitigation. Geothermics 53, 133–146. https://doi.org/10.1016/j.geothermics.2014.05.007.

Mignan, A., Werner, M.J., Wiemer, S., Chen, C.-C., Wu, Y.M., 2011. Bayesian Estimation of the Spatially Varying Completeness Magnitude of Earthquake Catalogs. Bull. Seismol. Soc. Am. 101 (3), 1371–1385. https://doi.org/10.1785/0120100223.

Mignan, A., Karvounis, D., Broccardo, M., Wiemer, S., Giardini, D., 2019b. Including seismic risk mitigation measures into the Levelized Cost of Electricity in enhanced geothermal systems for optimal siting. Appl. Energy 238, 831–850. https://doi.org/10.1016/j.apenergy.2019.01.109.

Mukuhira, Y., Dinske, C., Asanuma, H., Ito, T., Häring, M.O., 2017. Pore pressure behavior at the shut-in phase and causality of large induced seismicity at Basel, Switzerland. J. Geophys. Res. 122, 411–435. https://doi.org/10.1002/2016JB013338.

Panzera, F., Mignan, A., Vogfjord, K.S., 2017. Spatiotemporal evolution of the completeness magnitude of the Icelandic earthquake catalogue from 1991 to 2013. J. Seismol. 21, 615–630. https://doi.org/10.1007/s10950-016-9623-3.

Park, S., Kim, K.I., Xie, L., Yoo, H., Min, K.-B., Kim, M., Yoon, B., Kim, K.Y., Zimmermann, G., Guinot, F., Meier, P., 2020. Observations and analyses of the first two hydraulic stimulations in the Pohang geothermal development site, South Korea. Geothermics 88, 101905. https://doi.org/10.1016/j.geothermics.2020.101905.

Richter, B., Jónsson, S.S., Sigurdsson, O., 2001. Geldinganes, Rannsóknarhola RV-43 Úrvinnsla og Samantekt á Borgögnum. BR-SSJo-Omar-2001-01, Reykjavik Energy, p. 95. Technical Report20 Decemberpages.

Sæmundsson, K., Sigurgeirsson, M.Á., Hjartarson, Á., Kaldal, I., Kristinsson, S.G., Víkingsson, S., 2016. Geological Map of Southwest Iceland, 1:100000, 2nd edition. Icelandic Energy Research, Reykjavik. http://jardfraedikort.is/.

Steingrímsson, B., Friðleifsson, G.Ö., Gunnarsson, K., Thordarson, S., Þórhallson, S., Hafstað, Þ.H., 2001. Well RV-43 in Geldinganes: The terms for the well location and design. Orkustofnun, Reykjavík, Iceland. Technical report (In Icelandic).

Stober, I., 2011. Depth- and pressure-dependent permeability in the upper continental crust: data from the Urach 3 geothermal borehole, southwest Germany. Hydrogeol. J. 19, 685–699. https://doi.org/10.1007/s10040-011-0704-7.

Thorsteinsson, H., Gunnarsson, G., 2014. Induced Seismicity – Stakeholder Engagement in Iceland. GRC Trans. 38, 879–881.

Tomasson, J., Thorsteinsson, T., 1978. Drillhole stimulation in Iceland. In: Presented at ASME Energy Technology Conference & Exhibition, 5 November. Houston, TX, USA.

Trutnevyte, E., Wiemer, S., 2017. Tailor-made risk governance for induced seismicity of geothermal energy projects: an application to Switzerland. Geothermics 65, 295–312. https://doi.org/10.1016/j.geothermics.2016.10.006.

Tryggvason, A., Rögnvaldsson, S.T., Flovenz, Ó.G., 2002. Three-dimensional imaging of the P- and S-wave velocity structure and earthquake locations beneath southwest Iceland. Geophys. J. Int. 151 (3), 848–866. https://doi.org/10.1046/j.1365-246X.2002.01812.x.

Tulinius, H., Axelsson, G., Tómasson, J., Kristmanssdóttir, H., Gudmundsson, Á., 1996. Stimulation of well SN-12 in the Seltjarnarnes low-temperature field in SW-Iceland. In: Presented at 21st Workshop on Geothermal Reservoir Engineering. Stanford, CA, USA. Stanford University, 22-24 January.

van der Elst, N.J., Page, M.T., Weiser, D.A., Goebel, T.H.W., Hosseini, S.M, 2016. Induced earthquake magnitudes are as large as (statistically) expected. J. Geophys. Res. 121 (6), 4575–4590. https://doi.org/10.1002/2016JB012818.

van Elk, J., Doornhof, D., Bommer, J.J., Bourne, S.J., Oates, S.J., Pinho, R., Crowley, H., 2017. Hazard and risk assessments for induced seismicity in Groningen. Neth. J. Geosci. 96, s259–s269. https://doi.org/10.1017/njg.2017.37.

Waldhauser, F., Ellsworth, W.L., 2000. A double-difference earthquake location algorithm: method and application to the northern Hayward fault. Bull. Seismol. Soc. Am. 90 (6), 1353–1368. https://doi.org/10.1785/0120000006.

Westaway, R., Younger, P.L., 2014. Quantification of potential macroseismic effects of the induced seismicity that might result from hydraulic fracturing for shale gas exploitation in the UK. Q. J. Eng. Geol. Hydrol. 47, 333–350. https://doi.org/10.1144/qjegh2014-011.

Wiemer, S., Kraft, T., Trutnevyte, E., Roth, P., 2017. Good Practice" Guide for Managing induced seismicity in deep geothermal energy projects in Switzerland. ETH Zurich. https://doi.org/10.3929/ethz-b-000254161. Report.

Zang, A., Stephansson, O., Stenberg, L., Plenkers, K., Specht, S., Milkereit, C., et al., 2017. Hydraulic fracture monitoring in hard rock at 410m depth with an advanced fluid-injection protocol and extensive sensor array. Geophys. J. Int. 208 (2), 790–813. https://doi.org/10.1093/gji/ggw430.

Zang, A., Oye, V., Jousset, P., Deichmann, N., Gritto, R., McGarr, A., et al., 2014. Analysis of induced seismicity in geothermal reservoirs – an overview. Geothermics 52, 6–21. https://doi.org/10.1016/j.geothermics.2014.06.005.

Zang, A., Yoon, J.S., Stephansson, O., Heidbach, O., 2013. Fatigue hydraulic fracturing by cyclic reservoir treatment enhances permeability and reduces induced seismicity. Geophys. J. Int. 195 (2), 1282–1287. https://doi.org/10.1093/gji/ggt301.

Zang, A., Zimmermann, G., Hofmann, H., Stephansson, O., Min, K.-B., Kim, K.Y., 2019. How to Reduce Fluid-Injection-Induced Seismicity. Rock Mech. Rock Eng. 52, 475–493. https://doi.org/10.1007/s00603-018-1467-4.

Ziegler, M., Rajabi, M., Heidbach, O., Hersir, G.P., Ágústsson, K., Árnadóttir, S., Zang, A., 2016. The stress pattern of Iceland. Tectonophysics 674, 101–113. https://doi.org/10.1016/j.tecto.2016.02.008.

Further reading

Grigoli, F., Cesca, S., Krieger, L., Kriegerowski, M., Gammaldi, S., Horalek, J., Dahm, T., 2016. Automated microseismic event location using Master-Event Waveform Stacking. Sci. Rep. 6, 25744. https://doi.org/10.1038/srep25744.